European Journal of
Mineralogy
Open Access

Contact metamorphic reactions and fluid–rock interactions related to magmatic sill intrusion in the Guaymas Basin

Alban Cheviet[1,2]**, Martine Buatier**[2]**, Flavien Choulet**[2]**, Christophe Galerne**[1]**, Armelle Riboulleau**[3]**,
Ivano Aiello**[4]**, Kathleen M. Marsaglia**[5]**, and Tobias W. Höfig**[6,a]

[1]Faculty of Geosciences, University of Bremen, Klagenfurter Straße 2–4, 28359 Bremen, Germany
[2]Laboratoire Chrono-Environnement, UMR 6249, Université Franche-Comté,
16 route de Gray, 25000 Besançon, France
[3]Laboratoire d'Océanologie et de Géosciences, UMR 8187, Université de Lille, CNRS,
Université du Littoral Côte d'Opale, 59655 Villeneuve d'Ascq, France
[4]Moss Landing Marine Laboratory, 8272 Moss Landing Road, Moss Landing, CA 95039-9647, USA
[5]Dept. of Geological Sciences, California State University Northridge,
18111 Nordhoff St., Northridge, CA 91330-8266, USA
[6]International Ocean Discovery Program, Texas A&M University, 1000 Discovery Drive,
College Station, TX 77845, USA
[a]current address: Project Management Jülich, Jülich Research Centre GmbH, Forschungszentrum Jülich,
Schweriner Str. 44, 18055 Rostock, Germany

Correspondence: Alban Cheviet (alban.cheviet@univ-fcomte.fr)

Abstract. Igneous basaltic intrusions into young organic-rich sedimentary basins have a major impact not only on the carbon cycle but also on major and trace element transfers between deep and superficial geological reservoirs. The actively rifting Guaymas Basin in the Gulf of California, which was drilled by the International Ocean Discovery Program during Expedition 385, represents the nascent stage of an ocean characterized by siliceous organic-rich sediments (diatom ooze) intruded by a very dense network of basaltic sills. This study focuses on Site U1546 where the relatively high geothermal gradient (over $200\,^\circ\mathrm{C\,km^{-1}}$) induces early diagenetic transformations in both pore waters and sediments, involving sulfide, carbonate and silica. Geochemical and mineralogical characterizations of the sediment at sill contacts indicate that sulfides and silica polymorphs are the main phases impacted by contact metamorphism, being evident by a transition from opal-CT to quartz and pyrite to pyrrhotite, respectively. Mass balance calculations have been used to estimate mass transfers in metamorphic aureoles. In the top contact aureole, predominantly isochemical metamorphism is reflected by the presence of authigenic quartz and disseminated 20–50 μm sized pyrrhotite crystals, filling primary interstitial space, and partial dissolution of detrital feldspar grains. In the bottom contact aureole, quartz and euhedral pyrrhotite crystals occur, which are up to 4 times larger than those at the top contact. Significant metamorphism of sediments is observed in the lower contact aureole, where plagioclase recrystallizes around the detrital feldspars and locally euhedral pyroxenes are included in patches of carbonate cement; this suggests precipitation from carbon-rich fluids at temperatures (T) higher than $300\,^\circ\mathrm{C}$. The lower contact aureole also is more enriched in CaO, Na$_2$O, Fe$_2$O$_3$ and trace elements (Cu, As, Zn, etc.) compared to the upper contact. Based on these petrological investigations, a conceptual model of magma–sediment–fluid interaction is proposed distinguishing top and bottom contact processes. Initial contact metamorphism due to sill emplacement is characterized by dehydration reactions in sediments and crystallization of new minerals. It was followed by carbonate precipitation from the released fluids. At a final stage, the temperature re-equilibrated with the geothermal gradient and the rocks were further altered by hydrothermal fluids.

1   Introduction

Mafic sills intruding organic-rich sediments are commonly occurring at the transition between the early stages of rifting and the embryonic formation of ocean crust, as well as usually along volcanic rifted margins (Peron-Pinvidic et al., 2019; Sapin et al., 2021). Sill emplacement induces sediment heating, fluid advection and hydrothermal circulation, playing a pivotal role in the release of thermogenic products (CO_2 and CH_4) into the pore water (Aarnes et al., 2010). In the context of large igneous provinces (LIPs), large volumes of magma emplaced synchronously are synonymous with equally large simultaneous contact metamorphism processes leading to global warming and biotic crises (Svensen et al., 2004; Galerne and Hasenclever, 2019; Svensen et al., 2009; Heimdal et al., 2018).

When hot basaltic magmas (1000 to 1200 °C) intrude a significantly colder sedimentary (20 to 200 °C) host rock, heat is transferred and the sediment temperature increases up to 600–800 °C in some cases (Wang et al., 2007), corresponding to a high-temperature and relatively low-pressure contact metamorphism. The aureole thickness can be determined through proxies such as (1) vitrinite reflectance (% Ro), which is a measure of the degree of maturation of the organic matter (Sweeney and Burnham, 1990), or (2) the loss of organic matter content (expressed as total organic carbon, TOC wt %) related to its irreversible transformation to thermogenic gas. Studies of contact aureoles associated with sills emplaced in organic-rich host sedimentary rocks show thickness variations between 30 % and 200 % of the intrusion thickness (Aarnes et al., 2010; Raymond and Murchison, 1988). The thickness of the contact aureole mainly depends on the volume of the intrusion (i.e., lateral extent and thickness), which governs the initial amount of heat available to dissipate over time. However, many other parameters must be considered, including the composition, texture and porosity of the host sediments, as well as the initial geothermal gradient (Aarnes et al., 2010; Winkler, 1979).

Changes in inorganic sediment components during contact metamorphism could depend on other additional factors such as the activity of cations, the presence of fluids and the kinetics of reactions. Furthermore, both isochemical and metasomatic metamorphic reactions also lead to the modification of petrophysical properties of the host sediments and fracturation at the origin of sudden and tremendous fluid advection processes (Jamtveit et al., 2004; Zucchi et al., 2023).

The metamorphic and dehydration reactions associated with contact metamorphism depend on the nature and induration of the surrounding sediments (Aarnes et al., 2010; Li et al., 2016). These reactions can generate fluids and gases (H_2O, CO_2, SO_2, CH_4) associated with pore fluid pressure buildup and temperature gradient driving hydrothermal circulation. Under some conditions, the fluid pressure may ex-

ceed the hydrostatic pressure initiating hydrofracturing in the aureole, allowing sudden fluid release and pressure dissipation through an intense discharge (Aarnes et al., 2011a; Svensen et al., 2004; Zucchi et al., 2023). These fractures may cause vertical fluid migration that creates a conduit between the aureole and the seafloor (Simoneit et al., 1978; Simoneit and Lonsdale, 1982; Saxby and Stephenson, 1987; Fisher and Narasimhan, 1991; Svensen et al., 2007, 2020). While contact metamorphic processes in hard sedimentary host rocks are well documented and numerically simulated (Aarnes et al., 2010; Iyer et al., 2013; Galerne and Hasenclever, 2019), studies focusing on contact metamorphism processes due to sill emplacement in soft unconsolidated sediments remain unexplored in an active modern setting.

The Guaymas Basin in the Gulf of California (Mexico; Fig. 1a) is a young rift basin marked by active seafloor spreading and high sedimentation rates ranging from ~ 0.5 to $\sim 0.8\,\mathrm{m\,kyr^{-1}}$ (Teske et al., 2021a). Numerous off-axis sills have recently intruded sediments within the uppermost 300 m below the seafloor (Berndt et al., 2016; Teske et al., 2021a). Concurrent sedimentation and subseafloor subalkaline magma emplacement make the Guaymas Basin the best modern analogue to study the impact of magma–fluid–sediment interactions on carbon cycling and potential climate forcing effects, as well as elemental transfers at the subseafloor through mineral reactions that are driven by epithermal fluid circulation at the subseafloor. Despite key structural features being identified as markers of the contact aureole processes in the Guaymas Basin (i.e., vertical conduit rooting to the edge of sills), the role of metamorphic and dehydration reactions for the thermogenic gas mobilization remains unexplored in an active modern settings.

The geological processes outlined above connect the seafloor with the subseafloor and motivated International Ocean Discovery Program (IODP) Expedition 385 “Guaymas Basin Tectonics and Biosphere”. Scientific objectives of this expedition relevant to this study included (1) understanding the effect of basaltic sill emplacement on carbon mobilization and retention processes, (2) refining the role of hydrothermal alteration on the formation of authigenic minerals in the sediments, and (3) providing new geochemical and geophysical data to understand sill–sediment interactions in a young marine rift basin (Teske et al., 2018). Among the different drilling locations, Site U1546 cored about 500 m of sediment crosscut by a 74 to 76 m thick basaltic sill (Teske et al., 2021b). Hence, this site offers the opportunity to study the metamorphic aureole developed in the upper and lower contacts of a sill. The present study thus aims to (1) characterize the mineralogical assemblages at the sill–sediment contact zones at Site U1546 and the metamorphic aureole around this sill and (2) reconstruct the mineralogical reactions and their relative chronology for the different types of
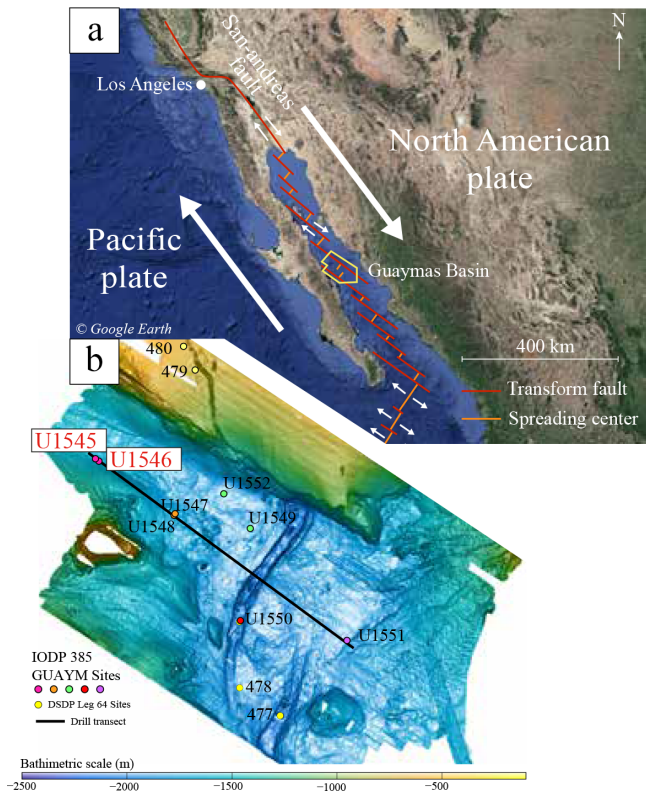
Figure 1. (a) Satellite view and tectonic setting of western North America and the Gulf of California. Modified from © Google Earth with information from Teske et al. (2021a). Yellow area shows the location of the map at the bottom. **(b)** Bathymetric map of Guaymas Basin, Mexico, with Baja California to the southwest, the Sonora margin to the northeast, and Deep Sea Drilling Project (DSDP) Leg 64 and IODP Expedition 385 sites, modified from Teske et al. (2021a).

interactions between magma, sediment and hydrothermal fluids.

2   Geological setting

The Guaymas Basin is located in the Gulf of California, straddling the Pacific–North American tectonic plate boundary (Fig. 1a). It initially formed via transtensional continental rifting, which ultimately led to the transfer of the Baja California peninsula from the North American Plate to the Pacific Plate ca. 12–15 Myr ago and the creation of new oceanic crust (Stock and Lee, 1994). The plate boundary in the central to southern Gulf of California consists of several narrow and comparatively short spreading segments in the form of axial troughs separated by transform faults (Fig. 1a).

Two spreading centers are found in the Guaymas Basin, physically manifested by graben structures developed in the sedimentary basin fill (Fig. 1b). Seismic observations of the northwestern Guaymas spreading segment indicate that the

continental rupture was complete by ca. 7 Ma and that new igneous (oceanic) crust formation has been accommodating Pacific and North American plate motion since that time (Lizarralde et al., 2007; Miller and Lizarralde, 2013). The formation of new oceanic crust is inferred from deep seismic profiles indicating seismic velocities matching those of typical oceanic crust. However, the relatively thick blanket of sediments deposited at high rates requires other geophysical methods to confirm the presence of new oceanic crust. The sedimentary succession consists of mainly organic-rich biogenic sediments derived from highly productive overlying waters and minor terrigenous sediments from the Baja California peninsula and Sonora margin (Einsele et al., 1980; Saunders et al., 1982), deposited at high rates ($\sim 1\,\mathrm{m\,kyr^{-1}}$; Teske et al., 2021a).

The northwestern Guaymas Basin is characterized by a large off-axis sill network emplaced at shallow depth (Berndt et al., 2016; Lizarralde et al., 2011). Additionally, the overall basin constitutes a regional heat flow anomaly (Goutorbe et al., 2011) that can be explained by discrete magma bodies emplaced in the sedimentary column (Neumann et al., 2023). Adjacent Sites U1545 and U1546 are only 1 km apart (Fig. 1b), and from these the oldest and thickest sediment successions (to ~ 540 m below seafloor (m b.s.f.)) intersected by IODP Expedition 385 were recovered. Site U1545, comprising three holes (A, B and C), constitutes the perfect reference location of a virtually undisturbed sediment succession, as it contained only a roughly 1 m thick sill recovered from 482.2 to 483.0 m b.s.f. (Teske et al., 2021c). The sediment succession at Site U1546, recorded by four holes (A, B, C and D), is mainly composed of clay-rich diatom ooze disrupted by a ~ 74–76 m thick sill located between 354.6 and 430.0 m b.s.f. (Teske et al., 2021b). The ~ 60 cm thick top and ~ 40 cm thick bottom intervals of this sill are composed of basaltic rock with xenoliths of sediment in contact with the adjacent sediment. The sill is marked by a transition from an aphanitic to a doleritic texture toward its center, and a ~ 12 m thick interval in the upper half of the intrusion is gabbroic (Teske et al., 2021b). This sill has a subalkaline chemistry indicating a mid-ocean ridge basalt (MORB) composition based on shipboard results (Teske et al., 2021c).

Previous studies of Site U1546 (Teske et al., 2021a; Lizarralde et al., 2023) have determined the thickness of the metamorphic aureole using organic matter as a proxy. The shipboard TOC values of the Guaymas Basin host sediments at Site U1546 vary between ~ 2 wt % and 5 wt %, while TOC decreases to zero in the samples located at the contact with the sill (Teske et al., 2021d). The thickness of the metamorphic aureoles on either side of the sill at Site U1546 has been estimated from changes in TOC measured in core samples and from the production index (PI). PI is calculated from source rock analyzer pyrolysis, with $\mathrm{PI} = S1\,/\,(S1 + S2)$, where S1 is the number of free hydrocarbons present in the rock and S2 is the number of hydrocarbons generated through cracking of organic matter (Es-

pitalié et al., 1985a; Peters, 1986). Oil- (0.1 < PI < 0.3) and wet-gas-generation (PI > 0.3) windows can be inferred from these data (Espitalie et al., 1985a, b, 1986; Peters, 1986). According to the TOC value of the sediments around the sill at Site U1546, the upper metamorphic aureole is about 15 m thick, while thickness of the lower aureole may reach 22 m. When considering PI values and evidence of metamorphism starting within the wet gas generation zone, the thickness of this aureole is reduced to 8 m above and 15 m below the sill. The very thin contact aureole thicknesses ($\leq 20\%$ of the sill thickness) have been attributed to the highly porous nature of the unconsolidated sediments found at these shallow depths of sill emplacement (Lizarralde et al., 2023).

3   Material and methods

3.1   Core description and sampling strategy

The biosiliceous sediment is relatively homogeneous in cored intervals of Holes U1546A and U1546C, suggesting that the sediment source distribution has been generally constant over time, being divided into four lithostratigraphic subunits during expedition IODP 385 (Teske et al., 2021a). These subunits, IA to ID, of the sediment succession are based only on the diagenetic evolution of the sediments (Fig. 2); similar subunits are also found at reference Site U1545 (Fig. 2; Teske et al., 2021a). The shallowest subunit, IA, is characterized by fine-grained sediment rich in diatom tests (diatom ooze) with subordinate detrital mud (quartz, feldspar and clay minerals). This lithology is present at Site U1546 up to 100 m b.s.f. (86 m b.s.f. at Site U1545). Subunit IB is composed of micrite-rich diatom clay. In addition to silt-sized micritic carbonate, centimetric dolomite concretions are also locally present in this subunit (Teske et al., 2021c). The transition between Subunits IB and IC is marked by the disappearance of dolomicrite at 197 m b.s.f. (220 m b.s.f. at Site U1545). Subunit IC is composed of clay-rich diatom ooze with diatom tests showing some traces of dissolution around 300 m b.s.f. At 320 m b.s.f. (352 m b.s.f. at Site U1545), Subunit ID is characterized by the disappearance of diatoms, i.e., biogenic opal-A and the occurrence of opal-CT. The resulting clay-rich lithology is also characterized by a higher degree of induration (siliceous claystone). At Site U1546, Subunit ID is crosscut by an igneous sill between 354.6 and 430 m b.s.f. (Hole U1546C).

The sampling strategy for this study was based on preliminary shipboard analyses carried out during IODP Expedition 385 such as TOC measurements and X-ray diffraction (XRD) analysis on bulk samples (Teske et al., 2021c). A total of 35 samples was collected at Site U1546 (from both Holes A and C) with most samples being located in the contact aureole (Fig. 2).

Samples above the sill at Site U1546 are distributed over a 72 m thick interval (from 282 m b.s.f. to the upper sill contact
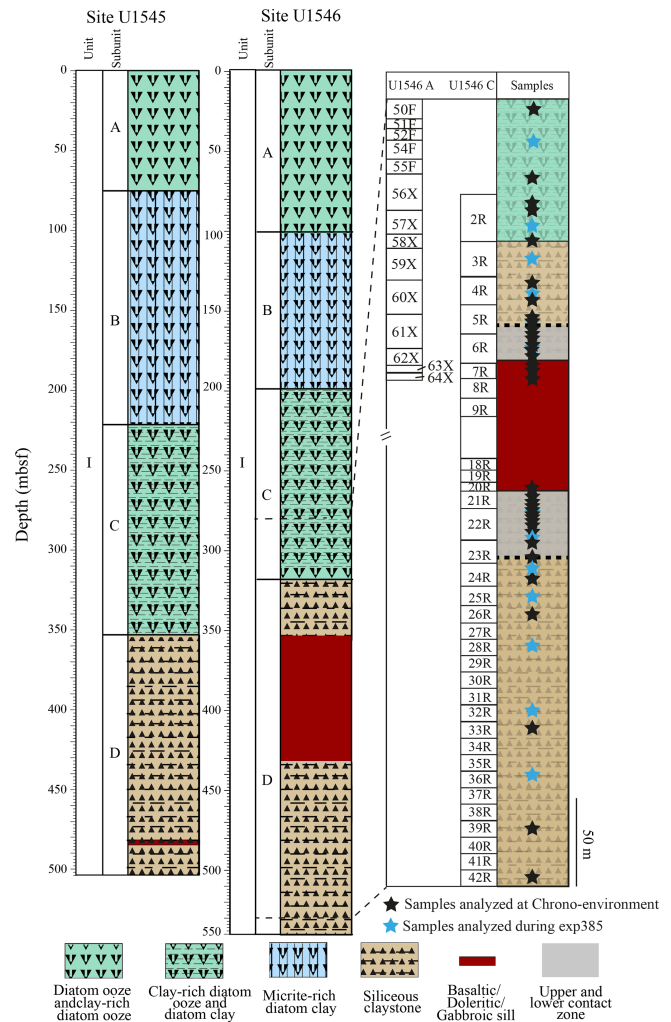

Figure 2. Lithostratigraphic columns of Sites U1545 and U1546 (1.1 km apart; Teske et al., 2021a). Sample distribution in Holes U1546A and U1546C: black stars represent the samples analyzed in this study, blue stars represent samples analyzed during Expedition 385 (Teske et al., 2021a).

at 354.6 m b.s.f.), with the sampling resolution increasing toward the sill. A similar sampling strategy was followed for the cores below the sill, in a stratigraphic interval of ~ 108 m (from 430 to 538 m b.s.f.; Fig. 2). Sediment xenoliths in the basaltic rocks located within the uppermost ~ 3 m of the sill were also collected (Fig. 2).

3.2   Analytical methods

The XRD analyses were conducted using a Bruker D8 Advance diffractometer on powders of 35 samples which were crushed using a Retsch PM 200 ball mill and further manually ground in an agate mortar. Analyses were run between 2 and $70°2\theta$ at 40 kV, 20 mA, using a CuKα radiation, a Ni filter, a step-scan of $0.02°$ and a step time of 1 s. EVA and Profex software were used for data processing

and phase determination. Thin sections of impregnated sediments and lithified sediment xenoliths were characterized using a numerical KEYENCE optical microscope (OM) and Thermo Fisher Apreo S scanning electron microscope (field emission gun scanning electron microscope, FEG-SEM). For SEM observations, thin sections were carbon-coated, and the images were acquired in high vacuum with a backscatter detector and an acceleration voltage of 30 kV. Energy-dispersive X-ray spectroscopy (EDS) provided qualitative analyses of the mineral composition. The fresh fractures of non-impregnated splits of some samples were also observed by SEM with a secondary electron detector at 5 kV. Major and trace elements were determined combining inductively coupled plasma atomic emission spectroscopy (ICP-AES) and ICP mass spectrometry (ICP-MS) methods after total digestion of bulk powdered samples with acids. Loss on ignition (LOI) was determined after heating the samples at $1000\,°C$ for 1 h. TOC was measured by HCl (25 %) leach at high temperature for 1 h to expel carbonates as CO_2, and the residue was analyzed for C by induction furnace on the same samples. All of these analyses were carried out at the laboratory ALS Dublin accredited to ISO / IEC 17025 : 2017 standards. The density of the samples was measured during Expedition 385 (Teske et al., 2021c). Plagioclase, pyroxene and sulfide minerals were analyzed through electron probe microanalysis (EPMA) on carbon-coated thin sections using a JEOL JXA-8530F Hyperprobe microprobe, equipped with five wave-dispersive X-ray spectrometers (WDSs) operating at 15 kV, with a beam current of 10 nA and a spot size of 1 µm.

3.3 Mass balance

To quantify mass transfer in the metamorphic aureoles we used mass balance calculations from Brimhall et al. (1991) and Oh and Richter (2005). Using the density values measured on the samples during Expedition 385 (Teske et al., 2021c) we can first calculate the coefficient of volume variation $\varepsilon_{i,w}$ relative to a protolith and then the transfer function $\tau_{j,w}$ for each chemical element for samples in the metamorphic aureoles. We consider zirconium as the immobile element reference. Index p corresponds to the protolith and w to the metasomatized material, ρ is the density of the material in $g\,cm^{-3}$, C_i is the concentration of the element considered immobile, and C_j is the concentration of a given chemical element.

$$\varepsilon_{i,w} = \left(\frac{\rho_p \times C_{i,p}}{\rho_w \times C_{i,w}} \right) - 1$$

$$\tau_{j,w} = \left(\frac{\rho_p \times C_{j,p}}{\rho_w \times C_{j,w}} \right) (\varepsilon_{i,w} + 1) - 1$$

The sedimentation is considered constant over time, and the chemical composition of the sediments can be considered as homogeneous as indicated by a standard deviation less than 2 %. Therefore, the mean of the sediments above and below

the sill are considered as the reference sediments (protolith; Supplement Table S1).

3.4 Macroscopic description of studied samples

All sediment samples studied were taken from cores representing Subunits IC and ID. Based on shipboard analyses (Teske et al., 2021b), the shallowest samples are clay-rich diatomaceous ooze with minor detrital quartz and feldspars, as well as framboidal pyrite. These sediments are rich in organic matter with TOC values between 2 wt % and 3 wt % (Teske et al., 2021c). Sedimentary laminae are commonly observed. Figure 3 shows seven representative core sections from Holes U1546A and U1546C from Subunit ID and close-up images of some of the intervals sampled for this study (Fig. 3a to f).

In the vicinity of the upper sill–sediment contact, the sediments indurate to gray-brown siliceous claystone and become darker close to the contact with highly altered subvolcanic rocks (Fig. 3b).

The first upper meters of the igneous sill (Sections U1546C-6R-1, U1546C-7R-1 and U1546A-62X-CC) present a mostly aphanitic basaltic texture characterized by a microcrystalline groundmass that hosts large, 2–3 mm plagioclase phenocrysts. The basaltic rock is finely crystallized at chilled margins with no evidence of magmatic glass, but the groundmass is highly altered as suggested by the occurrence of clay minerals (Teske et al., 2021c). A doleritic texture gradually develops within Section U1546C-7R-1, while a gabbroic texture starts below this interval and is observed throughout in the upper half of the sill body. The basaltic interval also contains numerous sedimentary xenoliths (Fig. 3c), which are detailed below.

The sediments sampled below the bottom contact of the sill at ~ 430 m b.s.f. (Section U1546C-21R-1) are completely indurated but porous (i.e., within 5 m from the bottom contact porosity ranges between 42.2 % and 44.7 %; Teske et al., 2021c). They appear very light in color with lighter patches (Fig. 3d). They become progressively darker and laminated further away from the sill (Fig. 3e). They are completely black at the base of Section U1546C-21R-2 at 433 m b.s.f. (Fig. 3f). Further downhole at 445 m b.s.f., well-indurated siliceous claystone comparable to the sediments above the sill was recovered.

Based on this macroscopic description, the lithologies of the sediment samples can be grouped as follows: (1) siliceous claystones which correspond to the background sedimentary rocks above and below the sill, (2) black indurated sediments at the upper contact with the sill (upper contact zone, from 349 to 354.6 m b.s.f.), (3) white and black indurated sediments without sedimentary structure at the lower contact with the sill (lower contact zone, from 430 to 446 m b.s.f.), and (4) lithified sediment xenoliths in the basaltic top and bottom contact.
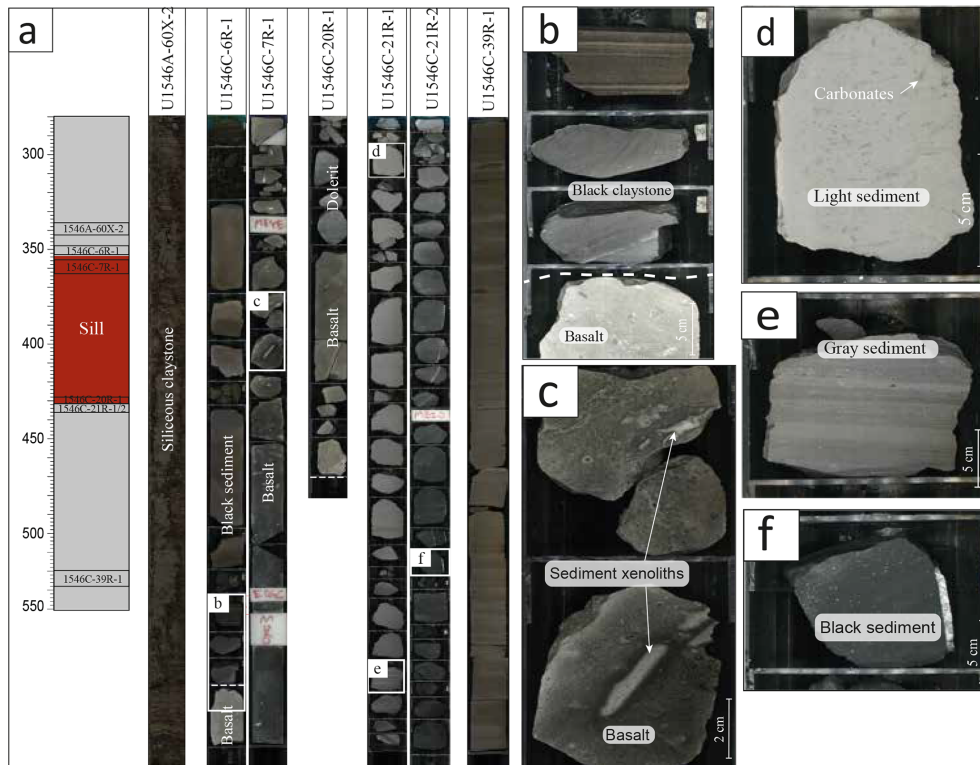
Figure 3. Characteristic changes in sediments above and below the sill and basaltic rocks for Holes U1546A and U1546C. **(a)** Core images from above and below the sill at Site U1546: U1546A-60X-2 corresponds to marine siliceous sediments, U1546C-6R-1 displays the upper sill–sediment contact marked by the dashed line in **(b)**, and U1546C-7R-1 corresponds to the top of the sill with numerous sedimentary xenoliths. U1546C-20R-1 is composed of magmatic rocks from the lower part of the sill, with texture changing from doleritic to basaltic. U1546C-21R-1 and U1546C-21R-2 are indurated sediments below the contact with the sill, and U1546C-39R-1 is indurated sediments. **(b)**, **(c)**, **(d)**, **(e)** and **(f)** correspond to close-up photos. **(b)** Close-up core photo of the upper basalt–sediment contact. **(c)** Sedimentary xenolith in Section U1546C-7R-1. **(d, e, f)** Contact zone below the sill composed of light to dark indurated sediments. Note that these images are of the archived halves of the core and that the equivalent intervals in the working halves were sampled.

4 Results

4.1 Bulk mineralogy and geochemistry

4.1.1 Geochemical data

Chemical data from the sediments and metasediments, along with the shipboard analyses, confirm that TOC values rapidly decrease from 345 m b.s.f. to nearly zero at the upper sill–sediment contact (Fig. 4a and Supplement Table S1). Under the sill, TOC also is low (from 1 wt %–2 wt % up to 446 m b.s.f.) in the white and black indurated sediments from the lower contact zone, but this value increases up to 3 wt % with outliers up to 6 wt % in the siliceous claystones (Fig. 4a). SiO_2 contents vary between 58 wt % and 70 wt % in the host sediments and the lower contact zone but reach up to 88 wt % in the upper contact zone (Fig. 4b). In the siliceous claystone, Na_2O and CaO values are 1 wt %–3 wt % and 2 wt %–5 wt %, respectively; these values decrease in the upper contact zone but reach up to 5 wt %–6 wt % Na_2O and 4 wt %–9 wt % CaO in the lower contact zone, with the ex-

ception of two samples of dolomite above the sill showing CaO content of 27 wt % (Fig. 4c). The K_2O values in sediments are between 1 wt %–3 wt % and decrease in the contact zone to reach 0.2 wt % in the lower contact zone (Fig. 4c). The host sediments are characterized by low iron content ($\sim$ 3 wt %), whereas the upper and lower contact zones can be enriched in iron (up to 6 wt %). There is a Fe_2O_3-rich layer at 434.26 m b.s.f. with an iron content of 15.5 wt % (Fig. 4d). The distribution of minor metals is heterogeneous in the lower contact zones with both depletion and local enrichment of Cu (up to 248 ppm) at 333 m b.s.f., as well as of As (up to 148 ppm) and Zn (up to 249 ppm) at 334 m b.s.f. (Fig. 4e–h).

4.1.2 Mass transfer

Volume variations in samples at the upper contact show no significant change except for two samples showing a maximum volume increase of $\sim$ 21 %–23 %. On the contrary, there is a significant volume decrease in the lower aureole ranging from 28 %–46 % (Table S1). At the sill–sediment
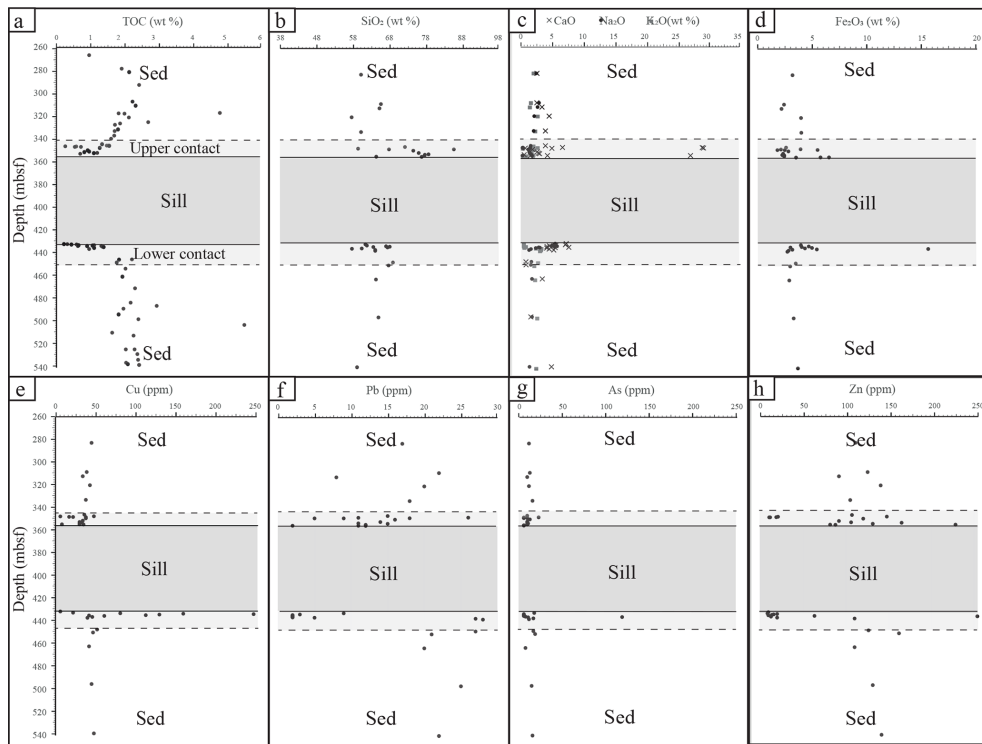
Figure 4. Characteristic downhole chemical evolutions of the samples at Site U1546, combining Holes U1546A and U1546C. Chemical data of sediments, samples in contact zones and basaltic rocks are displayed in Supplement Table S1. Unshaded intervals (Sed) are background sediment. Shaded areas represent the other three groups identified in the text: gray – upper and lower contact zones; dark gray – sill (mafic rock). TOC values are complemented by the values measured on shipboard (Teske et al., 2021c).
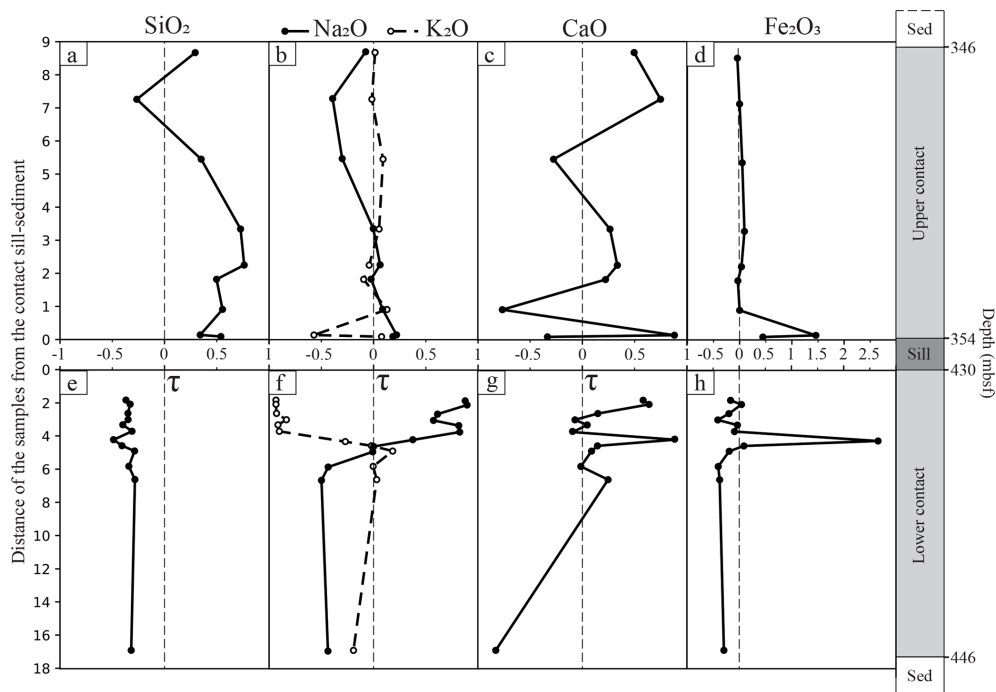

Figure 5. Mass balance calculations based on Brimhall et al. (1991). Circles represent transfer function τ for each sample as a function of the distance of the sample from the sill–sediment contact; a variation of $+0.5\,\tau$ represents a 50 % increase in the chemical element.

contact, there is a significant change in major-element content including SiO_2, Na_2O, K_2O, CaO and Fe_2O_3 (Figs. 4–5). In the upper contact, there is an input of SiO_2 leading to an increase of up to 80 % (Fig. 5a). There are small enrichments and depletions of K_2O which are balanced out in terms of the size of the aureole, and there is a loss of about 30 %–40 % of Na_2O (Fig. 5b). The distribution of CaO is heterogeneous with samples enriched and others depleted (Fig. 5c). Fe_2O_3 is immobile, with a significant input to the sediment just above the contact with the sill (Fig. 5d). In the lower contact zone, there is a loss of SiO_2 from the metamorphosed sediment (Fig. 5e). In contrast, there is an enrichment of 60 % CaO within the first 3 m of the lower contact and another rich layer at 434.26 m b.s.f. (Fig. 5g). Within the first 4 m from the bottom contact, there is also a total loss of K_2O and an enrichment of Na_2O. Below 434 m b.s.f. within the lower contact aureole K_2O is enriched and Na_2O is lost. At the scale of the lower aureole Fe_2O_3 is redistributed with a significant enrichment at 4.26 m from the contact (Fig. 5h).

4.1.3 Bulk XRD data

According to the bulk XRD data (Table 1), the siliceous claystones are mainly composed of silica of different forms, i.e., biogenic opal-A (Subunit IC) and diagenetic opal-CT (Subunit ID) (Fig. 6a and Table 1). Feldspars of various compositions, including plagioclase and orthoclase, as well as quartz, are also present as minor components. The siliceous claystone also contains minor pyrite and calcite. Opal-CT is detected downhole to 346 m b.s.f. (Table 1). Quartz is the only silica phase in XRD patterns from the sediments between 346 and 446 m b.s.f. in the upper and lower contact zones, but opal-CT is observed again below 446 m b.s.f. (Fig. S1). At the upper contact with the sill (between 346 and 354.6 m b.s.f.), quartz is a major phase in the black indurated sediments. Feldspars and carbonate minerals are also present. Iron sulfides occur in the form of pyrrhotite (Fig. 6b). In the white and black indurated sediments from the lower contact zone (430–446 m b.s.f.), quartz is always present (Fig. 6c). The characteristic feldspar (plagioclase) peaks (27.8°, 28°, 22° 2θ) in this altered material are more intense than in the host sediment XRD spectra, which means that they are probably more abundant and/or better crystallized. The white and black indurated sediments from the lower contact zone also contain pyrrhotite and augite-type pyroxene (Fig. 6c).

4.2 Petrological results (optical microscopy, SEM and microprobe analyses)

Based on bulk mineralogy and geochemistry data, petrological investigations are presented for each group of sediments and sedimentary rocks: host sediments, upper contact aureole, lower contact aureole and sedimentary xenoliths in the basaltic rock.
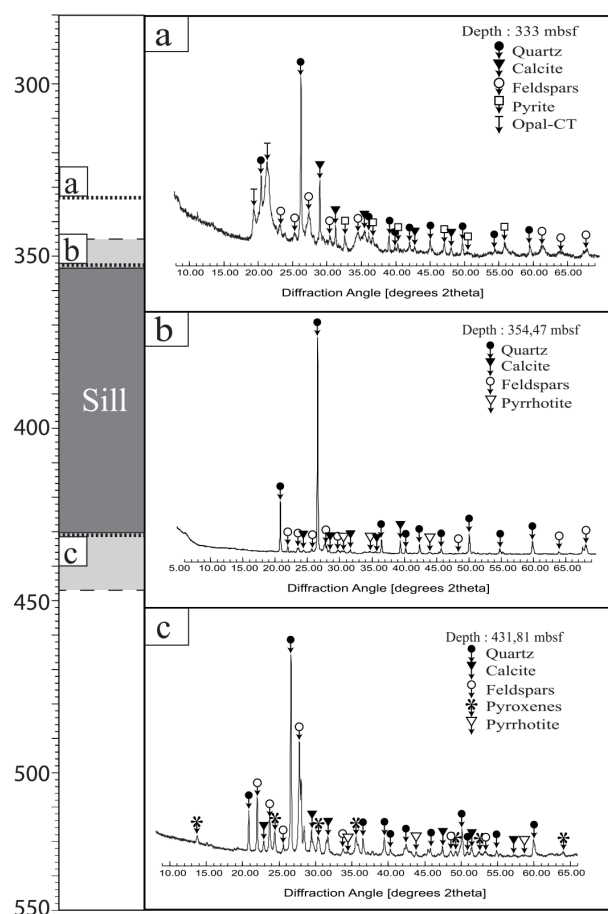

Figure 6. Representative XRD patterns of the studied sediments and metamorphic aureoles. **(a)** Background sediment (siliceous claystone) (Sample U1546A-60X-2, 70–72 cm); **(b)** upper contact zone (black indurated sediments) (Sample U1546A-62X-CC, 16–18 cm); **(c)** lower contact zone (white and black indurated sediments) (Sample U1546C-21R-1, 7–11 cm).

4.2.1 Host sediments (siliceous claystone)

At the microscale, siliceous claystone displays lamination characterized by the alternation of siliciclastic-rich and carbonate–opal-A-rich or carbonate–opal-CT-rich layers (Fig. 7a). The size of detrital feldspar and quartz grains ranges between $\sim$ 5 and 30 µm (Fig. 7b–c). Based on SEM and EDS analyses, feldspar chemical compositions are heterogenous, including Ca-rich to Na-rich plagioclase, as well as potassic feldspar (orthoclase). The matrix is composed of poorly crystallized detrital clay minerals (Fig. 7c). Pyrite is observed as disseminated framboids in the clay matrix (Fig. 7b) or forms framboids associated with calcareous microfossils (Fig. 7d). These latter ones are observed in the lighter laminae, which are mainly composed of authigenic carbonate and opal-CT. Minor barite and zircon were also observed.

Table 1. Mineral assemblages of the studied samples based on bulk powder XRD analyses and thin-section observations. The relative proportion (qualitative estimation) of minerals was determined by the relative height of the major XRD reflection of the major mineral phases. (*) minor, (**) medium, (***) major. Qtz – quartz; Fsp – feldspar; Pl – plagioclase; Px – pyroxene; Cal – calcite; Ank – ankerite; Dol – dolomite; Py – pyrite; Po – pyrrhotite.

| Sample	Depth (m b.s.f.)	Unit	Lithology	Detrital Qtz	Detrital Fsp	Opal-A	Opal-CT	Qtz	Pl	Px	Cal	Ank	Dol	Framboidal Py	Authigenic Py	Po
U1546A-50F-4-35/39	282.86	IC	Siliceous claystone	*	*	***								*		
U1546C-2R-1-32/34	308.52	IC	Siliceous claystone	*	*	***					*			*		
U1546A-57X-1-92/96	312.22	IC	Siliceous claystone	*	*	**					*			*		
U1546C-3R-2-69/72	320.11	IC	Siliceous claystone	*	*	*					*			*		
U1546A-60X-2-70/72	333	ID	Siliceous claystone	*	*		**							*		
U1546A-61X-4-95/97	345.95	ID	Siliceous claystone	*	*		*	*			*			*		
U1546A-61X-5-85/87	347.36	ID	Siliceous claystone		*			**			*			*		
U1546C-6R-1-31/38	347.54	ID	Dolomite cherts										***			
U1546C-6R-1-72/78	347.92	ID	Dolomite cherts										***			
U1546C-6R-1-84/88	348.04	ID	Black sediment		*			**			*				*	*
U1546C-6R-1-89/93	348.09	ID	Black sediment		*			**			*				*	*
U1546A-61X-6-114/116	349.16	ID	Black sediment		*			***			*				*	*
U1546A-62X-1-105/109	351.28	ID	Black sediment		*			***			*				*	*
U1546A-62X-2-64/70	352.36	ID	Black sediment		*			***			*				*	*
U1546A-62X-2-108/111	352.79	ID	Black sediment		*			***			**				*	*
U1546A-62X-3-68/70	353.71	ID	Black sediment		*			***			**	*			*	*
U1546A-62X-CC-10/14	354.41	ID	Dolomite cherts										***			
U1546A-62X-CC-16/18	354.47	ID	Black sediment		*			***			**	*				**
U1546A-62X-CC-22/24	354.53	ID	Black sediment		*			***			**	*				**
U1546C-7R-1-20/23	357.1	ID	Basalt						***	**						
U1546C-7R-1-42/47	357.33	ID	Basalt						***	**						
U1546C-7R-1-52/56	357.42	ID	Basalt						***	**						
U1546C-21R-1-7/11	431.81	ID	White sediment					***	***	**	**	**				***
U1546C-21R-1-35/39	432.06	ID	White sediment					***	***	**	**	**				**
U1546C-21R-1-89/95	432.61	ID	White sediment					***	***	**	***	*				**
U1546C-21R-1-127/133	432.99	ID	White sediment					***	**	*	***	*				**
U1546C-21R-2-12/16	433.3	ID	Gray sediment					***	**	*	***	*				**
U1546C-21R-2-50/56	433.69	ID	Black sediment					***	**	*	***	*				**
U1546C-21R-2-94/96	434.26	ID	Black sediment					***	*	*	***	*				**
U1546C-21R-2-138/140	434.56	ID	Black sediment					***	*	*	***	*				**
U1546C-22R-1-3/6	434.73	ID	Black sediment					***	*	*	***	*				**
U1546C-22R-1-18/21	434.88	ID	Black sediment					**	*		***	*				**
U1546C-22R-1-110/113	435.8	ID	Black sediment					**			***	*			*	*
U1546C-22R-2-48/51	436.6	ID	Black sediment					**			***	*			*	
U1546C-23R-2-97/99	446.89	ID	Black sediment				*				***	*			*	
U1546C-24R-1-34/36	449.44	ID	Siliceous claystone	*	*		***				**			*		
U1546C-26R-3-66/68	461.7	ID	Siliceous claystone	*	*		***				*			*		
U1546C-33R-2-34/37	494.78	ID	Siliceous claystone	*	*		***	***			*			*		
U1546C-39R-2-35/37	524.02	ID	Siliceous claystone		*			***			*			*		
U1546C-42R-2-35/37	538.19	ID	Siliceous claystone		**			***			*			*		
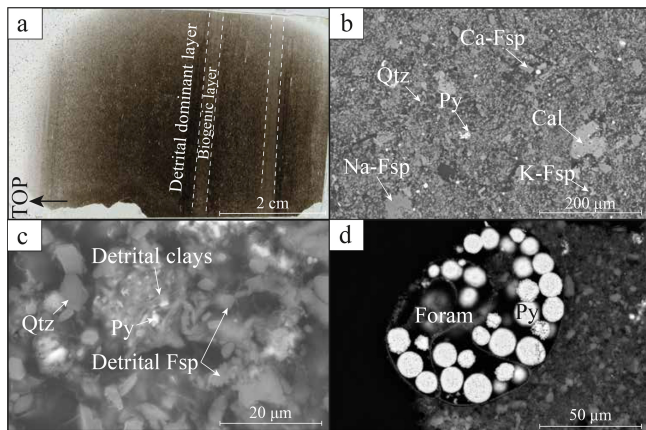
Figure 7. Optical microscope and SEM images of the background sediments. **(a)** Photomicrograph of a siliceous claystone (U1546A-61X-6, 114–116 cm); **(b, c, d)** backscattered SEM images of **(b)** texture of the siliceous claystone, **(c)** detrital clays and feldspars, and **(d)** framboidal pyrite in a foraminifer test. Mineral abbreviations: Qtz – quartz; Fsp – feldspars (Na-rich, Ca-rich and K-rich); Py – pyrite; Cal – calcite; and Foram – foraminifer.

4.2.2 The upper contact aureole

The black indurated metasediments of the upper aureole still display sedimentary laminae despite significant mineralogical changes (Fig. 8a). The siliciclastic laminae include feldspar and quartz. Feldspar composition ranges from Na-rich to Ca-rich plagioclase, and K-feldspar is present as well (Fig. 8a, b). SEM observations of freshly fractured surfaces show that feldspar is partially altered with dissolution along the cleavage planes. Euhedral authigenic quartz is observed under the SEM (Fig. 8c). The occurrence of newly formed clay minerals is attested by their textural arrangement (Fig. 8b) on the edges of newly formed quartz crystals or filling pore spaces. According to EDS analysis and clay mineral morphology, these clay minerals are rich in Mg and Fe and could correspond to corrensite (smectite and chlorite mixed layer; Welton, 1984; Buatier et al., 1995). Large detrital micas are locally altered to iron sulfides (Fig. 8d). Framboidal pyrite is still present at 348 m b.s.f. but surrounded by authigenic pyrite, suggesting possible partial transformation of framboidal pyrite into authigenic pyrite (Fig. 8e). Below 351 m b.s.f., authigenic pyrrhotite is the most abundant iron sulfide (Fig. 8f), but authigenic pyrite is still present down to 353.7 m b.s.f. Pyrrhotite becomes the only sulfide phase just above the basalt–sediment interface.

4.2.3 The lower contact aureole

The indurated sediments below the sill do not display any apparent sedimentary structures but show micrometric pore spaces. The major mineral phases are plagioclase and quartz. Plagioclase crystals are larger than in the upper contact zone
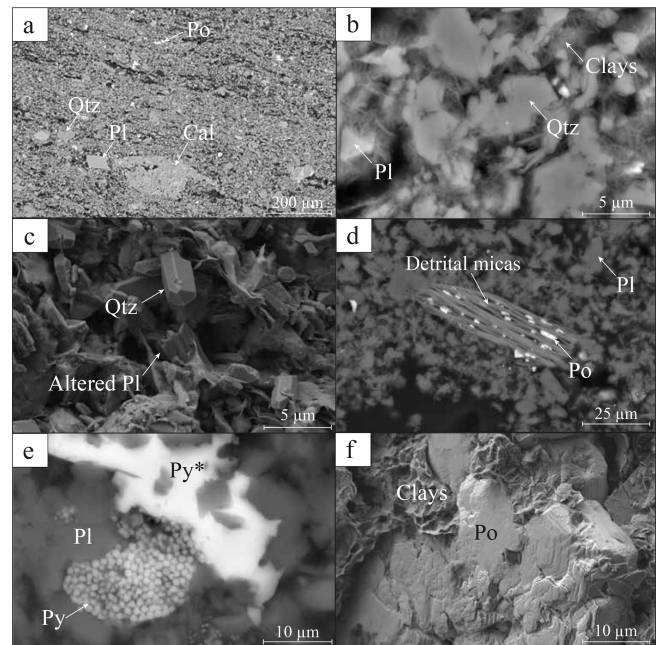

Figure 8. SEM images of sediment at upper contact zone (Sample U1546C-6R-1, 89–93 cm). **(a, b, c)** Backscattered images of the texture of the black indurated sediments observed by SEM, as well as secondary-electron (SE) SEM image on fresh breaks for **(c)**. **(d, e)** Backscattered image of **(d)** detrital micas in black indurated sediments and **(e)** formation of authigenic pyrite from framboidal pyrite. **(f)** SE image of pyrrhotite and authigenic clays in black sediments observed on fresh breaks. Mineral abbreviations: Qtz – quartz; Pl – plagioclase; Py – framboidal pyrite; Py* – authigenic pyrite; and Po – pyrrhotite.

($\sim$ 20–80 µm in size) and display well-developed euhedral shapes (Fig. 9a, b, e), with chemical zoning between the core and the rim (Fig. 9b). Based on microprobe analyses (Table S3), in the lower aureole, the plagioclase cores have heterogeneous composition between Ab_{20} and Ab_{90}. Conversely, between 430–434 m b.s.f., the rims are more homogenous ranging from Ab_{50} to Ab_{65} (Fig. 11a). Below 434 m b.s.f., feldspar rims have a potassic composition of Or_{78-98}. The euhedral shape of quartz crystals suggests that they are newly formed crystals. Patches of carbonates are disseminated throughout the metamorphosed sediments (Fig. 9c, d). The patches consist of a calcite–ankerite cement, with embedded quartz, plagioclase and euhedral pyroxene crystals (Fig. 9d). The pyroxene has diopside composition ($Wo_{0.5}$, $En_{0.3}$ and $Fs_{0.2}$; Fig. 11b). Well-crystallized phyllosilicate crystals up to 20–30 µm long fill the porosity (Fig. 9a). These clay minerals are never found as inclusions in the calcite cement, consistent with a later precipitation event.

The most abundant sulfides in the lower contact zone are represented by pyrrhotite, which appears as 200–300 µm sized euhedral crystals partly dissolved at their edge (Fig. 9e,

f) and commonly associated with the carbonate patches (Fig. 9e). The composition of pyrrhotite ranges between $Fe_{0.93}S$ and $Fe_{0.84}S$ (Fig. 11c). Closer to the sill pyrrhotite is the only sulfide mineral (Fig. 9f). At 433 m b.s.f., pyrrhotite partially transforms into chalcopyrite ($CuFeS_2$) and rarely Ni–Co–Fe sulfosalt. At 434.5 m b.s.f., arsenopyrite (FeAsS), chalcopyrite and galena (PbS) are found in association with pyrrhotite (Figs. 9g–11c). The occurrence of these base-metal-bearing minerals correlates with the enrichment in copper, arsenic and lead observed in bulk-rock chemistry (Figs. 5–6). Below 436 down to 446 m b.s.f., authigenic pyrite surrounding framboidal pyrite is found as in the upper aureole (Fig. 9h). Framboidal pyrite alone is found below 446 m b.s.f.

4.2.4 Xenoliths in basaltic rock

The sill samples from the upper sill–sediment contact (Samples U1546C-7R-1, 20–23 cm; U1546C-7R-1, 42–47 cm; and U1546C-7R-1, 52–56 cm) display a microlithic texture and contain centimetric xenoliths (Fig. 10a–c). These xenoliths display various mineral compositions. In Sample U1546C-7R-1, 42–47 cm, the xenolith is composed of plagioclase, quartz, clinopyroxene, pyrrhotite, calcite, ankerite and clay mineral crystals. Plagioclase is present as aggregates surrounded by quartz crystals (Fig. 10b). Pyrrhotite is disseminated throughout the xenolith. Locally, clay minerals and calcite fill the interstitial space between the quartz and plagioclase crystals. Clinopyroxene crystals are found at the edges of the xenolith. On the other hand, Sample U1546C-7R-1, 52–56 cm, contains a xenolith where euhedral clinopyroxene crystals are enclosed in quartz crystals (Fig. 10d). All these xenoliths present a dark-colored millimeter-thick contact zone with the surrounding host basaltic rock. This contact zone is composed of large plagioclase (500 μm), ilmenite ($FeTiO_3$) and clinopyroxene crystals (Fig. 10e). The size of the plagioclase and clinopyroxene crystals abruptly decreases toward the basaltic rock to reach that of the microlites. In sample U1546C-7R-1, 42/47 cm, feldspar of the xenolith is albitic, while the large plagioclase crystals in the contact zone have compositions ranging from Ab_{55} to Ab_{90}. Toward the contact with basaltic rock, as crystal size decreases, the composition of plagioclase becomes intermediate between those of microlites in the basaltic host and those of the contact zone plagioclase crystals (Fig. 11a).

Xenolith clinopyroxenes in Sample U1546-7R-1, 52/56 cm, have an augite composition. In the contact zone of samples U1546-7R-1, 52/56 cm, and U1546C-7R-1, 42/47 cm, sediment-hosted clinopyroxenes have a composition similar to that of microlites of the basaltic host (Fig. 11b). On the other hand, euhedral clinopyroxenes present in carbonate patches in the contact zone just below the sill are Fe-rich diopside, in contrast to the primary (magmatic) augite. These xenoliths are interpreted as having sedimentary origin due to their mineralogy and texture that
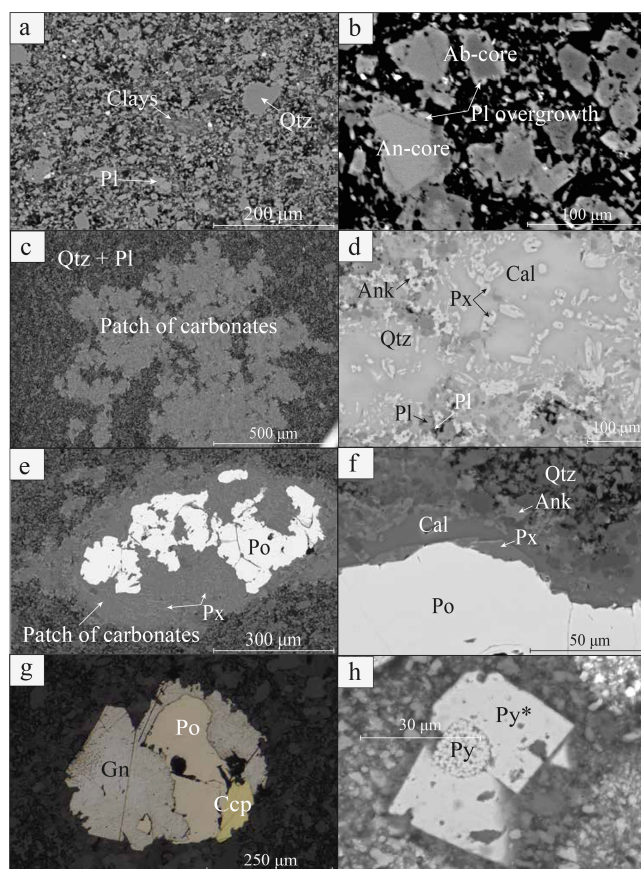

Figure 9. Backscattered SEM images of sediments at the lower contact zone (**a**, **b**, **c**, **d** and **e** correspond to Sample U1546C-21R-1, 7–11 cm, and **h** to Sample U1546C-21R-2, 138–140 cm). (**a, b**) Textures of the sediments and zonation in plagioclases with cores of various composition and homogenous overgrowth for (**b**); (**c, d**) patchy carbonates in sediments composed of calcite and ankerite, in thin sections; (**e**) pyrrhotite partially dissolved at its edges, embedded by pyroxenes and calcitic cement (patch of carbonates); (**f**) crystallization of pyroxenes and calcite at the edges of pyrrhotite; (**g**) images taken using reflected light microscopy; sulfides in white and black indurated sediments showing the precipitation of galena and chalcopyrite around pyrrhotite. (**h**) Backscattered SEM observation of authigenic pyrite (Py*) surrounding framboidal pyrite (Py). Mineral abbreviations: Qtz – quartz; Pl – plagioclase; Px – pyroxene; Cal – calcite; Ank – ankerite; Po – pyrrhotite; Gn – galena; and Ccp – chalcopyrite.

are very similar to the metamorphosed sediment from the lower contact zone described above.

5 Discussion

5.1 Metamorphic aureole characteristics

The chemical and mineralogical changes recorded by the sediments at Site U1546 show that quartz is present from the margins of the sill outwards before transitioning to opal-
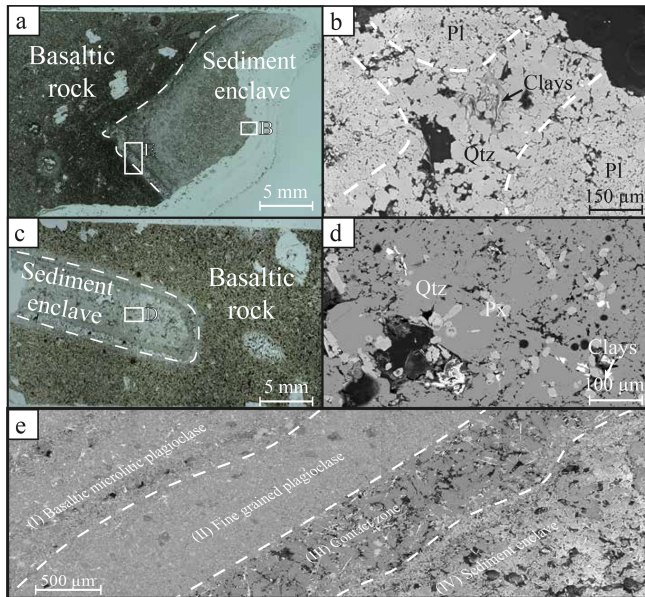
Figure 10. Optical microscope and backscattered electron SEM images of sediment xenoliths in basaltic rocks. **(a–c)** Photomicrographs of basalt with sediment enclaves (**a, b**: Sample U1546-7R-1, 42–47 cm; **c, d**: Sample U1546-7R, 52–56 cm). **(b–d)** SEM images of selected areas from the enclaves of **(a–c)**; **(e)** SEM image of the enclave-basaltic rock contact, which can be divided into four zones: (I) basaltic microlitic texture, (II) fine-grained plagioclase crystals, (III) contact zone and (IV) sediment enclave. The dashed lines represent the abrupt change in grains size. Mineral abbreviations: Qtz – quartz; Pl – plagioclase; Px – pyroxene; and Ank – ankerite.

CT between 8 m above the sill and 15 m below the sill. The pyrite–pyrrhotite transition is gradual with an intermediate zone where framboidal pyrite is converted into authigenic pyrite, and then pyrrhotite pseudomorphically replaces pyrite. The pyrite–pyrrhotite transition occurs close to the sill, 6 m above and below (Fig. 12). The depth interval of the opal-CT–quartz transition corresponds to both the gas-generation window (PI > 0.3) and the decrease in the TOC. The difference of thickness between the metamorphic aureoles could be related to differential thermal transfers from the sill. While sediments are mainly heated by thermal conduction and low-efficiency convection below the sill, fluid advection through the less lithified, more porous overburden is able to dissipate the heat more rapidly above the sill (Wang et al., 2007; Zhao et al., 2008; Lizarralde et al., 2023) resulting in a thinner aureole. The most significant difference between sills emplaced at depth in indurated sediments and the present study is the thickness of the aureoles. At Site U1546 the upper and lower metamorphic aureoles are 11 % and 23 %, respectively, of the thickness of the magmatic intrusion. This aureole thickness is very small compared to the size of metamorphic aureoles where the magma was emplaced in indurated rocks (Aarnes et al., 2011b). Furthermore, there are no current high-temperature minerals such as garnet, and
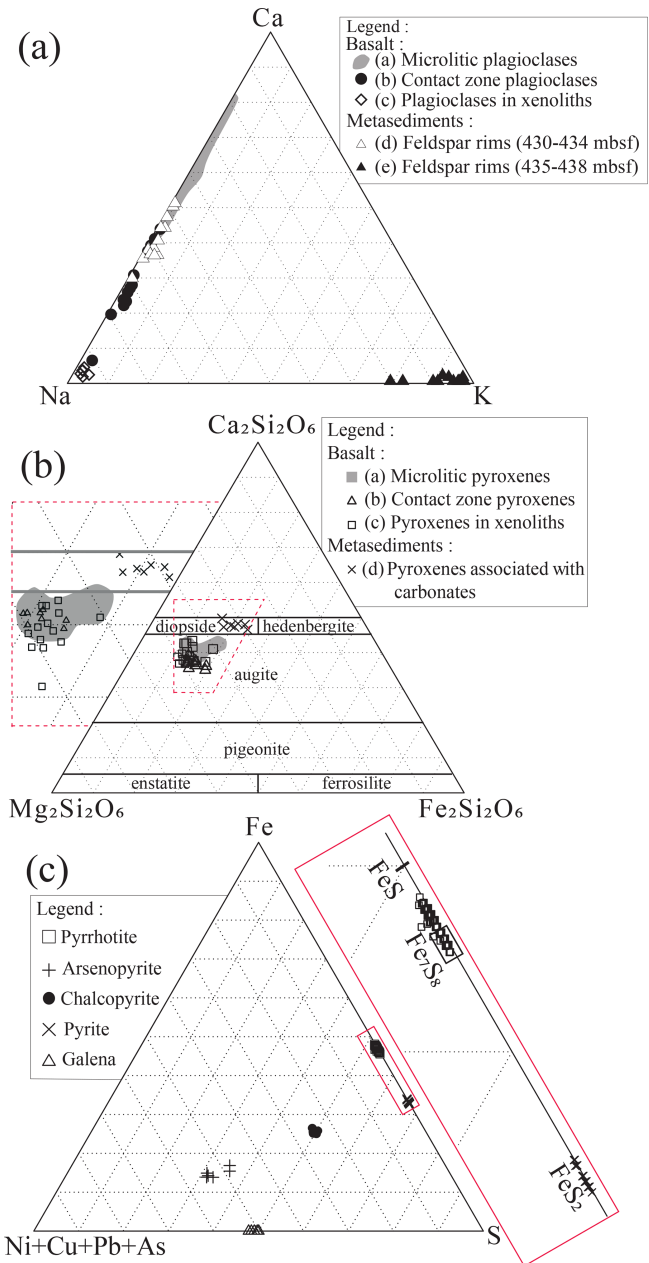

Figure 11. Chemical composition of plagioclases, clinopyroxenes and sulfides in basaltic rocks and sediments. **(a)** Na–Ca–K ternary classification diagram of feldspars with the analyses of plagioclases: microlites in basaltic rocks (a; the most calcic composition corresponds to the phenocrysts), plagioclases recrystallized at the xenolith-basaltic rocks contact (b), plagioclases in enclaves (c) and the chemical composition at the border of recrystallized plagioclases in sediments (d and e). **(b)** Ternary diagram of clinopyroxenes with the analyses on clinopyroxenes from basaltic rock (gray field, a), from the contact zone (b), within the enclaves (c) and within the metasediment (d). **(c)** Ni + Cu + Pb + As–Fe–S ternary diagram of the analyses on sulfides in the lower metamorphic aureole.

only clinopyroxenes were observed in the first 5 m of the lower aureole. These differences are essentially due to the petrophysical properties of the sediments in Guaymas Basin, where the magma is emplaced in porous ($\sim 60\,\%–70\,\%$), water-rich, unconsolidated sediments that will rapidly dissipate the heat released by the sill, limiting the size of the metamorphic aureoles and the formation of high-temperature mineralogical assemblages.

Figure 12 summarizes the mineralogical variations in the top and bottom metamorphic aureoles. The occurrence and conditions of formation of each mineral phase are discussed below.

Silica is abundant in the Guaymas Basin sediments in the form of biogenic silica (opal-A) in the shallowest sediments. Sites U1545 and U1546 (~ 1 km apart) display the same lithologic record of middle to late Pleistocene (≤ 0.44 Ma) sediments composed of laminated diatom oozes and clay minerals. Both sites also have similar geothermal gradients (about $220–230\,°\mathrm{C\,km}^{-1}$), porewater silica concentration profile and diatom test preservation trends with depth (Teske et al., 2021c). At both sites, there is a transition from a relatively soft diatom ooze (Subunit IC) to a harder and more brittle porcelanite (Subunit ID). It starts between ~ 320 m and ~ 350 m b.s.f. and corresponds to the opal-A to opal-CT transition. This transition is systematically reflected in the petrophysical data by a more pronounced reduction in porosity with increasing depth, combined with a more pronounced increase in density (Teske et al., 2021a, b). The similar depth of the opal-A to opal-CT transition at both Sites U1546 and U1545 (Fig. 2) suggests that this transition has an unequivocal diagenetic origin and is not related to contact metamorphism.

While the natural progression of the opal-A–opal-CT transition (above the sill at ~ 320 m b.s.f.) postdates the overprint of the heat of the contact aureole, the occurrence of euhedral quartz crystals in the upper and lower aureole around the sill is clearly related to the thermal input by the sill at the time of its emplacement. The opal-CT–quartz transition is observed at 8 m above the sill and 16 m below the sill. This suggests dissolution–precipitation processes pointing to biogenic and diagenetic opal phases in the host sediment being dissolved and reprecipitated as crystalline micro- to macro-quartz from Si-rich fluid. Thus, the quartz occurrence in the direct vicinity of the sill is evidence of intense heat dissipated during cooling and crystallization of the sill.

The host sediments contain framboidal pyrite, and its formation is related to early diagenetic processes implying the degradation of organic matter and anaerobic oxidation of methane, both coupled to sulfate reduction. Indeed, organic matter is the site of sulfide production by sulfate reducing bacteria and iron precipitation in the form of pyrite microcrystals which aggregate to form a framboid (Wilkin and Barnes, 1997).

In the contact aureole, euhedral pyrite and pyrrhotite are both present. The formation of pyrrhotite in metasediments is generally related to elevated temperature under anoxic conditions (Rochette et al., 2001; Wang and Salveson, 2005). In sedimentary basins, the occurrence of pyrrhotite may be an indication of burial temperatures exceeding $200\,°\mathrm{C}$ (Crouzet et al., 2001). Several studies reported the formation of pyrrhotite in thermal aureoles of magmatic intrusions (Gillett, 2003; Wehland et al., 2005; Ledevin et al., 2012; Aubourg et al., 2014). At Site U1546, pyrite is present down to 350 m b.s.f. and pyrrhotite is only found in the 6 m close to the top sill contact. Pyrrhotite is found below the sill to a depth of 436 m b.s.f. Authigenic (hydrothermal) pyrite is present at the outer margin of the contact aureole and can be considered as a transitional phase between framboidal pyrite and pyrrhotite. The transition zones are located between 348 and 353 m b.s.f. in the upper aureole and between 436 and 446 m b.s.f. in the lower aureole. The mechanism by which the framboids are converted into euhedral crystals is not well understood (Ostwald and England, 1979). Several studies suggest that euhedral pyrite grains are the product of crystal overgrowth on framboid microcrystals in the presence of organic matter and/or fluids rich in iron and sulfur during later fluid circulations (Large et al., 2007; Ostwald and England, 1979; Sawlowicz, 1993; Soliman and El Goresy, 2012). It is important to note that pyrrhotite is absent in sediments from Site U1545. This is consistent with the $\sim 220–230\,°\mathrm{C\,km}^{-1}$ temperature gradient in this area of the Guaymas Basin, which precludes the occurrence of diagenetic pyrrhotite at 350 m b.s.f. Pyrrhotite crystals present in the metamorphic aureoles can thus be related to an early stage of sediment heating during the sill emplacement. In the upper aureole, detrital feldspar crystals are partially dissolved, whereas in the lower aureole, feldspar overgrowths are observed on detrital feldspar rims. The feldspar overgrowths display homogenous compositions with albite-rich compositions between 430–434 m b.s.f. and potassic composition between 435–440 m b.s.f. Plagioclase recrystallization is also observed in the contact zone around the sediment xenoliths in the basaltic rocks. Plagioclase formed in the contact zone and in the xenoliths as the result of sediment transformation with pore fluid precipitation being more albitic in composition than plagioclase microlites in the basaltic rocks.

Newly formed pyroxene occurs in the sediment xenoliths as well as in some metamorphosed sediments located in the lower aureole at 5 m downhole from the sill contact. They are generally small euhedral crystals included in authigenic quartz cement or more commonly in carbonate cements. Pyroxene is a common mineral in contact metamorphism such as in some hornfels facies (Aarnes et al., 2010; Svensen et al., 2010) and generally formed in the metamorphic aureole close to the intrusion (Winter, 2021). The crystallization of these pyroxenes requires a sufficient activity of CO_2 to form these anhydrous phases (Cui et al., 2003). High CO_2 concentration can be produced by decarboxylation but also by the catagenesis of the organic matter during early heat-driven reactions. Similar mineral assemblages were described in skarn
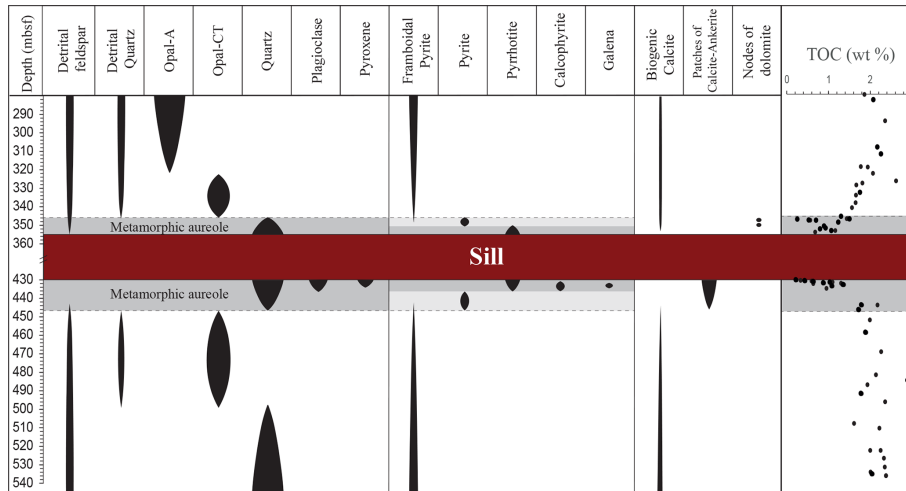
Figure 12. Synthesis of mineral evolution downhole through the section drilled at Site U1546. Limits are established according to XRD data and complemented by the thin-section observations.

environments where authigenic pyroxene (augite), quartz and pyrrhotite formed during a prograde stage (Cui et al., 2003; Jiménez-Franco et al., 2020; Marincea et al., 2020; Meinert et al., 2005). The Guaymas Basin sediments in the contact aureoles registered this early stage metamorphic/metasomatic event, but their mineralogical assemblages differ from those of the skarns by the occurrence of plagioclase and the absence of wollastonite and garnet. These differences can be explained by (1) the nature of the host sediments, (2) the composition of the intrusive magma, and (3) the temperature and the duration of the heating event.

5.2 Mineral transformation and fluid mobilization

Among the main mineralogical changes in the metamorphic aureoles at Site U1546, we can highlight the occurrence of newly formed quartz and pyrrhotite. The opal-CT is destabilized to form quartz shortly after the sill emplacement following Eq. (1).

$$SiO_2 \cdot nH_2O \rightarrow SiO_2 + nH_2O \tag{1}$$

This dehydration reaction releases a large amount of water into the system in addition to the pore water initially present. In addition, CO_2 and CH_4 are released in the metamorphic aureoles from organic matter and biogenic carbonates. Indeed, the cracking of organic matter releases methane according to Eq. (2).

$$C_xH_y \rightarrow C_{x'} + nCH_4 \tag{2}$$

The sedimentary carbonates are dissolved, which releases CO_2 into the aureoles.

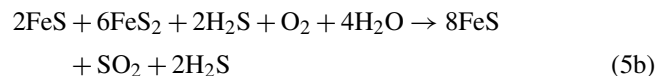$$CaCO_3 + 2H^+ \rightarrow Ca^{2+} + CO_2 + H_2O \tag{3}$$
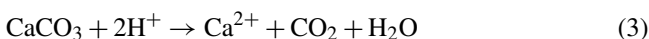
In metamorphic environments pyrite breaks down to pyrrhotite under reducing conditions and releases sulfur

(Tomkins, 2010; Yallup et al., 2013) following Eq. (4).

$$2FeS_2 \rightarrow 2FeS + S_2 \tag{4}$$

However, two other chemical reactions may contribute to the precipitation of pyrrhotite. Water liberated by the dehydration of silicates can dissolve pyrite and other components leading to the consumption of pyrite to maintain equilibrium (Yallup et al., 2013) according to the following reactions.

$$8FeS_2 + 2H_2O \rightarrow 2FeS + 6FeS_2 + 2H_2S + O_2 \tag{5a}$$

$$2FeS + 6FeS_2 + 2H_2S + O_2 + 4H_2O \rightarrow 8FeS$$
$$+ SO_2 + 2H_2S \tag{5b}$$

These reactions are considered significant above 400 °C (Yallup et al., 2013).

In the presence of carbon, the following reaction may also be observed.

$$2H_2O + C + 2FeS_2 \rightarrow CO_2 + 2H_2S + 2FeS \tag{6}$$
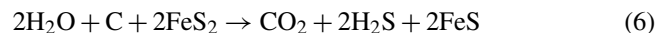
In the Guaymas Basin, the sediments are rich in organic matter. Close to the contact with the sill, the organic matter is cracked, releasing methane and carbon dioxide into the system, thus enabling Eq. (6). The dissolution of opal-CT also produces water, which promotes Eqs. (5a), (5b) and (6). The water produced by the opal-CT–quartz transition serves as the foundation for forming authigenic clay minerals (corrensite in the upper aureole), but it can also leave this system through open hydrothermal vents observed at the seafloor (Teske et al., 2021b). As the sills in this environment are often considered impermeable to epithermal fluid flow (Galerne and Hasenclever, 2019), the migration of fluids produced by the reactions in the lower aureole is only possible laterally below the sill or they remain trapped together with gas below the sill if they are produced too far

from the sill edges. Fluid accumulation below the sill supports Eq. (5) in the lower metamorphic aureole. The transformation of pyrite into pyrrhotite depends on the temperature (Fig. 13a) but also on pH and the fugacities of sulfur and oxygen (Toulmin and Barton, 1964; Hayba et al., 1985). As the fugacity of sulfur decreases (low sulfidation), the pyrite–pyrrhotite transformation is reached more quickly (Fig. 13a). From Fig. 13b, it emerges that the transition is favored under reducing conditions from interaction with acidic fluids and, under more oxidized conditions, from interaction with alkaline fluid. Neutral to slightly alkaline and low-oxidation conditions also facilitate the precipitation of pyrrhotite (Hayba et al., 1985; Fig. 13b).

The distribution of feldspars in the lower aureole suggests that fluid flow allowed the remobilization and transport of chemical elements. Indeed, we have evidence for metasomatism, which contributes to the crystallization of sodium-rich plagioclase within the first 4 m from the lower sill–sediment contact and potassium feldspars in the next meters. According to our mass balance calculations, we observe a complete leaching of K_2O and an enrichment in Na_2O close to the sill (between 430–434 m b.s.f.). Below 434 m b.s.f., there is a depletion in Na_2O and an enrichment in K_2O (Fig. 5). Although we cannot exclude the possibility of original variations in the protolith, it is highly probable that fluids were involved in the redistribution of the alkaline elements. These metasomatic fluids first leached the detrital feldspars to become concentrated in potassium close to the contact. K-feldspar further precipitates below 434 m b.s.f. where the conditions are favorable (higher activity and temperature). Since plagioclases precipitate at higher temperatures compared to K-feldspars, they are observed near the sill, as they are more stable in its vicinity (Jamieson and O'Beirne-Ryan, 1991; Blum, 1994).
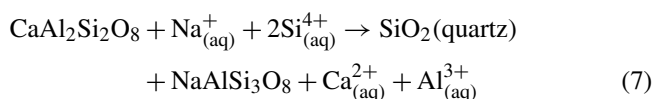
Fluid remobilization in the lower contact zone is also attested by the distribution of base metals (Zn, Cu, As) measured in the bulk sediments and the transformation of pyrrhotite into chalcopyrite, arsenopyrite and/or galena. During contact metamorphism the cracking of the organic matter releases CO_2 into the system and the Mg and Ca available in pore fluids, and the destabilization of pyrite releases Fe. All these features (Mg, Ca, Fe and CO_2) may contribute to the precipitation of pyroxenes and carbonate patches, mainly ankerite and calcite around pyrrhotite (Fig. 14f).

According to the mass balance calculations, there is no external source of chemical elements from either the sill or the sediments. Within the system, fluids can circulate and remobilize the elements and create horizons, which are more or less enriched in metal-bearing sulfides and carbonates. However, it can be hypothesized that metamorphic fluids rich in carbon, major elements and metals produced during contact metamorphism were trapped below the sill, which is considered to be impermeable, and facilitated the recrystallization of silicates, carbonates and sulfides. In contrast, in the upper aureole the fluids could escape from the system, which

is why only temperature-related phase changes (opal-CT to quartz and pyrite to pyrrhotite) are observed.

5.3 Sediment–magma mingling and associated metasomatic reactions

In settings similar to the Guaymas Basin, magmas emplaced in unconsolidated, wet host sediments form mingling facies generally called peperites. They show a wide spectrum of textures and mineral phases. This process may trigger hydro-magmatic explosions, as well as sediment fluidization, and generate variable degrees of sediment assimilation into the magma (Galerne et al., 2006; Skilling et al., 2002; White et al., 2000). Assuming that the sedimentation rates and the regional heat flow did not change significantly with time and space, it can be shown that the depth of emplacement of the sill at Site U1546 was controlled by the opal-A–opal-CT transition. This constrains the depth intervals of our samples at the deepest level of possible peperite formation. This also has an influence on the dynamics of magma emplacement. Whilst hydromagmatic explosion may not be possible near 325–350 m b.s.f., magma–sediment mingling may occur and result in the formation of decimetric sediment xenoliths, which are locally preserved in the basaltic rock samples from the upper part of the sill. The mineralogical assemblage of the sedimentary xenoliths reflects heat-driven dehydration reaction at temperatures higher than $300\,°C$ as suggested by the occurrence of contact metamorphic pyroxenes. Around the xenoliths, a clast–matrix interface is composed of recrystallized plagioclase, pyroxene and ilmenite as the result of metasomatic reactions. In this interval, plagioclase minerals have intermediate compositions between magmatic plagioclase and detrital plagioclase from the xenolith. This transition suggests that metasediments trapped in the magmas have been heated, dehydrated and further affected by chemical exchange between the altered basaltic rock and the sediment clasts in the contact zone. According to our petrological observations, quartz crystallization and feldspar albitization could be explained by Eqs. (7) and (8).

$$CaAl_2Si_2O_8 + Na^+_{(aq)} + 2Si^{4+}_{(aq)} \rightarrow SiO_2(quartz)$$
$$+ NaAlSi_3O_8 + Ca^{2+}_{(aq)} + Al^{3+}_{(aq)} \qquad (7)$$

Sediment xenoliths are recrystallized, detrital feldspars are albitized, and excess silica from the destabilization of biogenic silica precipitates as quartz around the albite nodules. Around the xenoliths, fine-grained plagioclases crystals are depleted in calcium because of albitization (Eq. 8).

$$CaAl_2Si_2O_8 + Na^+_{(aq)} + SiO_2 + 4H^+ \rightarrow NaAlSi_3O_8$$
$$+ Ca^{2+}_{(aq)} + Al^{3+}_{(aq)} + 2H_2O \qquad (8)$$
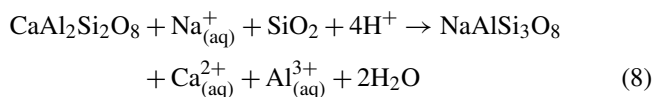
The destabilization of plagioclases in xenoliths and in the basaltic matrix contributes to the formation of authigenic plagioclase in the contact zone with an intermediate composition. A similar process is observed for the pyroxene of the
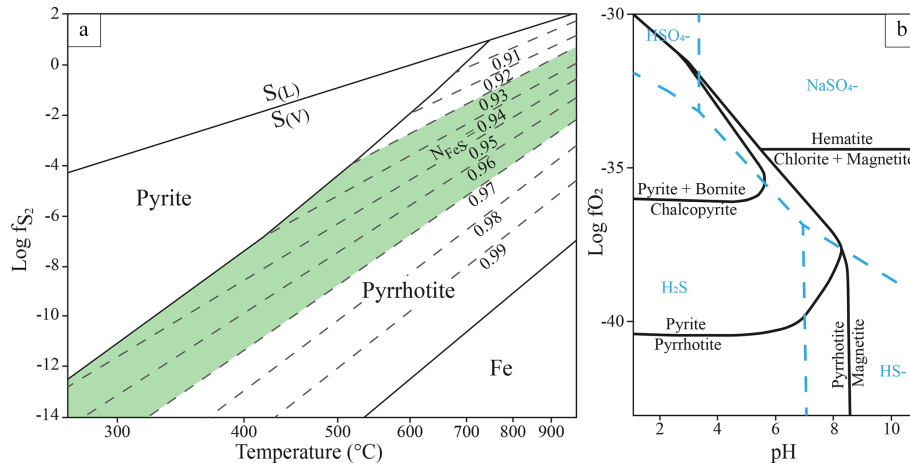
Figure 13. (a) Composition of pyrrhotite in the iron–sulfur system as a function of temperature and fugacity of S2. N_{FeS} is the mole fraction of FeS in the system, FeS-S2, at 1 kbar, modified from Toulmin and Barton (1964). Green area represents the N_{FeS} calculated for the pyrrhotites below the sill (Table S4). **(b)** Stability domains of sulfides as a function of fO_2 and pH; the dashed blue line represents the speciation of sulfur in a fluid as a function of fO_2 and pH at 250 °C and 50 bar, modified from Hayba et al. (1985).
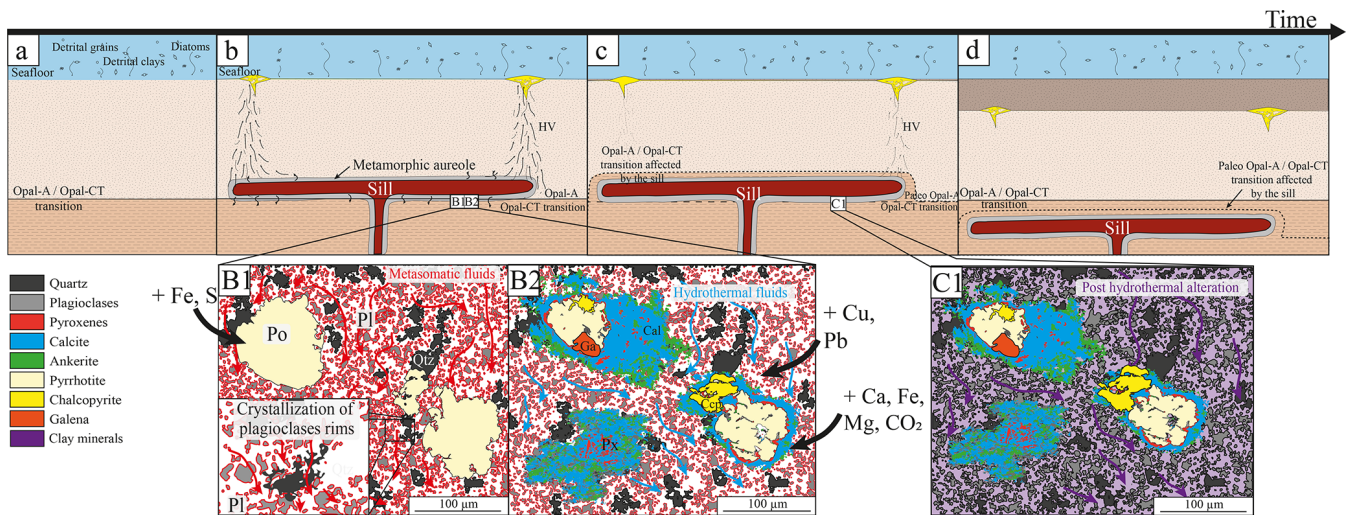
Figure 14. Stratigraphic model showing the succession of metamorphic reactions and fluid–sediment–basalt interactions in the metamorphic aureole in the Guaymas Basin sediments. **(a)** Stage before sill intrusion, with the sedimentation of biosiliceous sediment and transformation of opal-A into opal-CT by burial diagenesis. **(b)** Sill emplacement at the opal-A–opal-CT transition with contact metamorphism in the sediments around the sill: HV – hydrothermal vent. (B1) Crystallization of quartz and pyrrhotite in the sediments with the formation of rims around the plagioclases. (B2) Hydrothermal fluids that allow crystallization of clinopyroxenes, remobilizing metals and forming chalcopyrite and galena at the expense of pyrrhotite and precipitation of patches of carbonates. **(c, C1)** Late-stage alteration that forms clay minerals in sediments and basaltic rock. **(d)** Recent opal-A–opal-CT transition overprints the opal-A–opal-CT transition affected by the sill intrusion.

basaltic matrix and the xenoliths, since pyroxene in the contact zone has an intermediate composition.

The xenoliths of Sample U1546C-7R-1-52/56 cm have a different composition (quartz plus pyroxenes), but a similar contact zone is observed (texture and mineralogy). The difference in mineralogical composition compared to the other two samples may only be due to a slight difference in the composition of the sedimentary protolith.

Metasomatic reactions occur at the millimeter scale in metasediment xenoliths, but similar reactions are found at the sill–sediment contacts and probably occur at the basin scale. Indeed, in the lower contact zone and particularly 5 m below the sill, newly formed pyroxene (diopside) and feldspar overgrowth are present in the metasediments. The presence of authigenic pyroxene suggests the activity of relatively high-temperature fluids (>300 °C) (Zürcher et al., 2004).

5.4 Conceptual model of sediment–magma interaction in the lower contact aureole

Figure 14 summarizes the major sediment–magma and fluid interactions in the lower contact aureole indicated by this study. It is suggested that the sill emplacement occurs above the diagenetic opal-A–opal-CT boundary (Fig. 14a, b) because this diagenetic transition also is the first rheological transition below the seafloor. Plagioclase overgrowth, pyroxene, authigenic quartz filling the porosity and large pyrrhotite crystals are the result of precipitation from fluid with input of Fe and S to the heated sediments at temperatures $>300\,^\circ C$ (Fig. 14e). Locally in the lower aureole, pyrrhotite is partially altered and transformed into chalcopyrite and glaucodot, implying hydrothermal fluid circulation and the input of Cu and Pb. Conversely, calcite and ankerite cements are secondary phases formed by hydrothermal fluid circulation with the input or the redistribution of Ca, Fe and CO_2 (Fig. 14f). The occurrence of phyllosilicates in the pore space of the contact aureole suggests that fluid released by the different mineralogical reactions and/or late circulation of fluid enabled a rehydration of the sill and contact sediment (Fig. 14d–g).

6 Conclusions

The Guaymas Basin is a rare modern example where interaction between active sedimentation and magmatism can be studied in a nascent ocean basin. Off-axis Site U1546 provided an excellent recovery of top and bottom sediment–sill interfaces and enabled the study of the corresponding metamorphic aureoles. The 74 to 76 m thick sill first intersected intruded clay-rich diatom oozes at 354.6 m b.s.f. Based on mineralogy, chemistry and the texture of the sediments, we have shown that the sediments around the sill are affected by contact metamorphism. The main phases impacted by heating and dehydration processes are silica polymorphs, sulfides, feldspars and carbonates, with the respective transformations of opal to quartz and pyrite to pyrrhotite, as well as crystallization of plagioclases and precipitation of carbonates in the metasediments around the sill. The upper and lower aureoles display differences in thickness, texture and composition. The upper aureole is 8 m thick and still exhibits sedimentary lamination and contains detrital grains. On the contrary, in a 16 m zone under the sill, the metasediments display gradational changes becoming less altered with depth away from the sill, showing significant alteration of sediments near the sill contact, such as the recrystallization of plagioclase around detrital feldspars, local clinopyroxene crystallization and partial cementation by carbonates (calcite and ankerite). An enrichment in major (Fe) and trace elements (Cu, As, Zn) in the lower aureole combined with sulfide replacement processes suggests hydrothermal fluid circulation and recrystallization of metal sulfides. Identified sediment xenoliths record early magma–sediment interactions at high temper-

ature. These xenoliths suggest that partial sediment assimilation by the magma during its emplacement is possible, but there is no evidence of significant chemical contamination of the magma by the sediments.

The present study demonstrates that the contact aureoles are affected not only by the maturation of organic matter and dehydration reaction but also by mineralogical reactions concerning all sediment components (silica, silicates, sulfides, carbonates, organic matter), possibly resulting from the combination of different stages of alteration during and after the sill emplacement. Volatiles released by the dehydration of the sediments and the cracking of the organic matter influenced the physicochemical conditions (e.g., fO_2, fS_2, pH and temperature – T), which allowed the precipitation of minerals in the aureoles such as quartz, pyrrhotite and carbonates. The released fluids were therefore trapped in the metamorphic aureoles.

This study focused on an isolated sill in soft sediments in the Guaymas Basin, where the dominant mechanism is contact metamorphism to the detriment of assimilation processes. This dominant mechanism maintains a large storage of volatiles in the lithosphere. In other cases where magmatic productivity (volume of magma and duration of magmatism) is higher (e.g., Norilsk, Kambala, Raglan, Sudbury) assimilation mechanisms are dominant (Lesher, 2017; Arndt and Jenner, 1986; and references therein), potentially leading to the release of volatiles to more superficial reservoirs such as the ocean or the atmosphere. The mechanisms that allow the assimilation of large quantities of sediment and the release or storage of large quantities of volatiles need more investigations.

Author contributions. AC carried out the analyses and wrote the manuscript draft under the supervision of MB and FC. CG, AR, IA, KM and TWH reviewed and edited the manuscript. MB, CG, AR, IA, KM and TWH also contributed to the manuscript through their role as members of the shipboard science party on IODP Expedition 385.

References

Aarnes, I., Svensen, H., Connolly, J. A. D., and Podladchikov, Y. Y.: How contact metamorphism can trigger global climate changes: Modeling gas generation around igneous sills in sedimentary basins, Geochim. Cosmochim. Ac., 74, 7179–7195, https://doi.org/10.1016/j.gca.2010.09.011, 2010.

Aarnes, I., Svensen, H., Polteau, S., and Planke, S.: Contact metamorphic devolatilization of shales in the Karoo Basin, South Africa, and the effects of multiple sill intrusions, Chem. Geol., 281, 181–194, https://doi.org/10.1016/j.chemgeo.2010.12.007, 2011a.

Aarnes, I., Svensen, H., Polteau, S., and Planke, S.: Contact metamorphic devolatilization of shales in the Karoo Basin, South Africa, and the effects of multiple sill intrusions, Chem. Geol., 281, 181–194, https://doi.org/10.1016/j.chemgeo.2010.12.007, 2011b.

Arndt, N. T. and Jenner, G. A.: Crustally contaminated komatiites and basalts from Kambalda, Western Australia, Chem. Geol., 56, 229–255, https://doi.org/10.1016/0009-2541(86)90006-9, 1986.

Aubourg, C., Techer, I., Geoffroy, L., Clauer, N., and Baudin, F.: Detecting the thermal aureole of a magmatic intrusion in immature to mature sediments: a case study in the East Greenland Basin (73° N), Geophys. J. Int., 196, 160–174, https://doi.org/10.1093/gji/ggt396, 2014.

Berndt, C., Hensen, C., Mortera-Gutierrez, C., Sarkar, S., Geilert, S., Schmidt, M., Liebetrau, V., Kipfer, R., Scholz, F., Doll, M., Muff, S., Karstens, J., Planke, S., Petersen, S., Böttner, C., Chi, W.-C., Moser, M., Behrendt, R., Fiskal, A., Lever, M. A., Su, C.-C., Deng, L., Brennwald, M. S., and

Lizarralde, D.: Rifting under steam – How rift magmatism triggers methane venting from sedimentary basins, Geology, 44, 767–770, https://doi.org/10.1130/G38049.1, 2016.

Blum, A. E.: Feldspars in Weathering, in: Feldspars and their Reactions, edited by: Parsons, I., Springer Netherlands, Dordrecht, 595–630, https://doi.org/10.1007/978-94-011-1106-5_15, 1994.

Brimhall, G. H., Christopher J., L., Ford, C., Bratt, J., Taylor, G., and Warin, O.: Quantitative geochemical approach to pedogenesis: importance of parent material reduction, volumetric expansion, and eolian influx in lateritization, Geoderma, 51, 51–91, https://doi.org/10.1016/0016-7061(91)90066-3, 1991.

Buatier, M. D., Früh-Green, G. L., and Karpoff, A. M.: Mechanisms of Mg-phyllosilicate formation in a hydrothermal system at a sedimented ridge (Middle Valley, Juan de Fuca, Contrib. Mineral. Petrol., 122, 134–151, https://doi.org/10.1007/s004100050117, 1995.

Crouzet, C., Rochette, P., and Ménard, G.: Experimental evaluation of thermal recording of successive polarities during uplift of metasediments, Geophys. J. Int., 145, 771–785, https://doi.org/10.1046/j.0956-540x.2001.01423.x, 2001.

Cui, X., Nabelek, P. I., and Liu, M.: Reactive flow of mixed CO_2-H_2O fluid and progress of calc-silicate reactions in contact metamorphic aureoles: insights from two-dimensional numerical modelling: CO_2-H_2O FLUID FLOW and CALC-SILICATE REACTIONS, J. Metamorph. Geol., 21, 663–684, https://doi.org/10.1046/j.1525-1314.2003.00475.x, 2003.

Einsele, G., Gieskes, J. M., Curray, J., Moore, D. M., Aguayo, E., Aubry, M.-P., Fornari, D., Guerrero, J., Kastner, M., Kelts, K., Lyle, M., Matoba, Y., Molina-Cruz, A., Niemitz, J., Rueda, J., Saunders, A., Schrader, H., Simoneit, B., and Vacquier, V.: Intrusion of basaltic sills into highly porous sediments, and resulting hydrothermal activity, Nature, 283, 441–445, https://doi.org/10.1038/283441a0, 1980.

Espitalie, J., Deroo, G., and Marquis, F.: La pyrolyse Rock-Eval et ses applications, Deuxième partie., Rev. Inst. Fr. Pét., 40, 755–784, https://doi.org/10.2516/ogst:1985045, 1985a.

Espitalie, J., Deroo, G., and Marquis, F.: La pyrolyse Rock-Eval et ses applications, Première partie., Rev. Inst. Fr. Pét., 40, 563–579, https://doi.org/10.2516/ogst:1985035, 1985b.

Espitalie, J., Deroo, G., and Marquis, F.: La pyrolyse Rock-Eval et ses applications, Troisième partie., Rev. Inst. Fr. Pét., 41, 73–89, https://doi.org/10.2516/ogst:1986003, 1986.

Fisher, A. T. and Narasimhan, T. N.: Numerical simulations of hydrothermal circulation resulting from basalt intrusions in a buried spreading center, Earth Planet. Sc. Lett., 103, 100–115, https://doi.org/10.1016/0012-821X(91)90153-9, 1991.

Galerne, C., Caroff, M., Rolet, J., and Le Gall, B.: Magma–sediment mingling in an Ordovician rift basin: The Plouézec–Plourivo half-graben, Armorican Massif, France, J. Volcanol. Geotherm. Res., 155, 164–178, https://doi.org/10.1016/j.jvolgeores.2006.03.030 2006.

Galerne, C. Y. and Hasenclever, J.: Distinct Degassing Pulses During Magma Invasion in the Stratified Karoo Basin – New Insights From Hydrothermal Fluid Flow Modeling, Geochem. Geophy. Geosy., 20, 2955–2984, https://doi.org/10.1029/2018GC008120, 2019.

Gillett, S. L.: Paleomagnetism of the Notch Peak contact metamorphic aureole, revisited: Pyrrhotite from magnetite + pyrite under submetamorphic conditions: pyrrhotite from mag-

netite at notch peak, Utah, J. Geophys. Res., 108, B9, https://doi.org/10.1029/2002JB002386, 2003.

Goutorbe, B., Poort, J., Lucazeau, F., and Raillard, S.: Global heat flow trends resolved from multiple geological and geophysical proxies, Geophys. J. Int., 187, 1405–1419, https://doi.org/10.1111/j.1365-246X.2011.05228.x, 2011.

Hayba, D. O., Bethke, P. M., Heald, P., and Foley, N. K.: Geologic, Mineralogic, and Geochemical Characteristics of Volcanic-Hosted Epithermal Precious-Metal Deposits, in: Geology and Geochemistry of Epithermal Systems, Vol. 2, edited by: Berger, B. R. and Bethke, P. M., Soc. Econ. Geol., 2, 250–252, https://doi.org/10.5382/Rev.02.07, 1985.

Heimdal, T. H., Svensen, Henrik. H., Ramezani, J., Iyer, K., Pereira, E., Rodrigues, R., Jones, M. T., and Callegaro, S.: Large-scale sill emplacement in Brazil as a trigger for the end-Triassic crisis, Sci. Rep., 8, 141, https://doi.org/10.1038/s41598-017-18629-8, 2018.

Iyer, K., Rüpke, L., and Galerne, C. Y.: Modeling fluid flow in sedimentary basins with sill intrusions: Implications for hydrothermal venting and climate change: Fluid Flow In Sedimentary Basins, Geochem. Geophy. Geosy., 14, 5244–5262, https://doi.org/10.1002/2013GC005012, 2013.

Jamieson, R. A. and O'Beirne-Ryan, A. M.: Decompression-induced growth of albite porphyroblasts, Fleur de Lys Supergroup, western Newfoundland, J. Metamorph. Geol., 9, 433–439, https://doi.org/10.1111/j.1525-1314.1991.tb00537.x, 1991.

Jamtveit, B., Svensen, H., Podladchikov, Y. Y., and Planke, S.: Hydrothermal vent complexes associated with sill intrusions in sedimentary basins, Geol. Soc. Lond. Spec. Publ., 234, 233–241, https://doi.org/10.1144/GSL.SP.2004.234.01.15, 2004.

Jiménez-Franco, A., Canet, C., Alfonso, P., González-Partida, E., Rajabi, A., and Escalante, E.: The Velardeña Zn–(Pb–Cu) skarn-epithermal deposits, central-northern Mexico: New physical-chemical constraints on ore-forming processes, Boletín de la Sociedad Geológica Mexicana, 72, A270719, https://doi.org/10.18268/BSGM2020v72n3a270719, 2020.

Large, R. R., Maslennikov, V. V., Robert, F., Danyushevsky, L. V., and Chang, Z.: Multistage Sedimentary and Metamorphic Origin of Pyrite and Gold in the Giant Sukhoi Log Deposit, Lena Gold Province, Russia, Econ. Geol., 102, 1233–1267, https://doi.org/10.2113/gsecongeo.102.7.1233, 2007.

Ledevin, M., Arndt, N., Cooper, M. R., Earls, G., Lyle, P., Aubourg, C., and Lewin, E.: Intrusion history of the Portrush Sill, County Antrim, Northern Ireland: evidence for rapid emplacement and high-temperature contact metamorphism, Geol. Mag., 149, 67–79, https://doi.org/10.1017/S0016756811000537, 2012.

Lesher, C. M.: Roles of xenomelts, xenoliths, xenocrysts, xenovolatiles, residues, and skarns in the genesis, transport, and localization of magmatic Fe-Ni-Cu-PGE sulfides and chromite, Ore Geol. Rev., 90, 465–484, https://doi.org/10.1016/j.oregeorev.2017.08.008, 2017.

Li, X., Wang, Q., Zhang, W., and Yin, H.: Contact metamorphism of shales intruded by a granite dike: Implications for shale gas preservation, Int. J. Coal Geol., 159, 96–106, https://doi.org/10.1016/j.coal.2016.03.016, 2016.

Lizarralde, D., Axen, G. J., Brown, H. E., Fletcher, J. M., González-Fernández, A., Harding, A. J., Holbrook, W. S., Kent, G. M., Paramo, P., Sutherland, F., and Umhoefer, P. J.: Variation in styles of rifting in the Gulf of California, Nature, 448, 466–469, https://doi.org/10.1038/nature06035, 2007.

Lizarralde, D., Soule, S. A., Seewald, J. S., and Proskurowski, G.: Carbon release by off-axis magmatism in a young sedimented spreading centre, Nat. Geosci., 4, 50–54, https://doi.org/10.1038/ngeo1006, 2011.

Lizarralde, D., Teske, A., Höfig, T. W., González-Fernández, A., and IODP Expedition 385 Scientists: Carbon released by sill intrusion into young sediments measured through scientific drilling, Geology, 51, 329–333, https://doi.org/10.1130/G50665.1, 2023.

Marincea, Ş., Dumitraş, D.-G., Sava, C., Hatert, F., and Dal Bo, F.: Mineralogy of a High-Temperature Skarn, in High CO_2 Activity Conditions: The Occurrence from Măgureaua Vaţei (Metaliferi Massif, Apuseni Mountains, Romania), Minerals, 10, 677, https://doi.org/10.3390/min10080677, 2020.

Meinert, L. D., Dipple, G. M., and Nicolescu, S.: World Skarn Deposits, One Hundredth Anniversary Volume, Soc. Econ. Geol., 299–336, https://doi.org/10.5382/AV100.11, 2005.

Miller, N. C. and Lizarralde, D.: Thick evaporites and early rifting in the Guaymas Basin, Gulf of California, Geology, 41, 283–286, https://doi.org/10.1130/G33747.1, 2013.

Neumann, F., Negrete-Aranda, R., Harris, R. N., Contreras, J., Galerne, C. Y., Peña-Salinas, M. S., Spelz, R. M., Teske, A., Lizarralde, D., Höfig, T. W., and Expedition 385 Scientists: Heat flow and thermal regime in the Guaymas Basin, Gulf of California: Estimates of conductive and advective heat transport, Basin Res., 35, 12755, https://doi.org/10.1111/bre.12755, 2023.

Oh, N.-H. and Richter, D. D.: Elemental translocation and loss from three highly weathered soil–bedrock profiles in the southeastern United States, Geoderma, 126, 5–25, https://doi.org/10.1016/j.geoderma.2004.11.005, 2005.

Ostwald, J. and England, B. M.: The relationship between euhedral and framboidal pyrite in base-metal sulphide ores, Mineral. Mag., 43, 297–300, https://doi.org/10.1180/minmag.1979.043.326.13, 1979.

Peron-Pinvidic, G., Manatschal, G., and the "IMAGinING RIFTING" Workshop Participants: Rifted Margins: State of the Art and Future Challenges, Front. Earth Sci., 7, 218, https://doi.org/10.3389/feart.2019.00218, 2019.

Peters, K. E.: Guidelines for Evaluating Petroleum Source Rock Using Programmed Pyrolysis, Bulletin, 70, 318–329, https://doi.org/10.1306/94885688-1704-11D7-8645000102C1865D, 1986.

Raymond, A. C. and Murchison, D. G.: Development of organic maturation in the thermal aureoles of sills and its relation to sediment compaction, Fuel, 67, 1599–1608, https://doi.org/10.1016/0016-2361(88)90202-5, 1988.

Rochette, P., Lorand, J.-P., Fillion, G., and Sautter, V.: Pyrrhotite and the remanent magnetization of SNC meteorites: a changing perspective on Martian magnetism, Earth Planet. Sc. Lett., 190, 1–12, https://doi.org/10.1016/S0012-821X(01)00373-9, 2001.

Sapin, F., Ringenbach, J.-C., and Clerc, C.: Rifted margins classification and forcing parameters, Sci. Rep., 11, 8199, https://doi.org/10.1038/s41598-021-87648-3, 2021.

Saunders, A., Fornari, D., Joron, J. L., and Tarney, J.: Geochemistry of basic igneous rocks, Gulf of California, Deep-Sea Drill. Project Leg., 64, 595–642, 1982.

Sawlowicz, Z.: Pyrite framboids and their development: a new conceptual mechanism, Geol. Rundsch., 82, 148–156, https://doi.org/10.1007/BF00563277, 1993.

Saxby, J. D. and Stephenson, L. C.: Effect of anigneous intrusion on oil shale at Rundle (Australia), Chem. Geol., 63, 1–16, https://doi.org/10.1016/0009-2541(87)90068-4, 1987.

Simoneit, B. R. T. and Lonsdale, P. F.: Hydrothermal petroleum in mineralized mounds at the seabed of Guaymas Basin, Nature, 295, 198–202, https://doi.org/10.1038/295198a0, 1982.

Simoneit, B. R. T., Brenner, S., Peters, K. E., and Kaplan, I. R.: Thermal alteration of Cretaceous black shale by basaltic intrusions in the Eastern Atlantic, Nature, 273, 501–504, https://doi.org/10.1038/273501a0, 1978.

Skilling, I. P., White, J. D. L., and McPhie, J.: Peperite: a review of magma–sediment mingling, J. Volcanol. Geotherm. Res., 114, 1–17, https://doi.org/10.1016/S0377-0273(01)00278-5, 2002.

Soliman, M. F. and El Goresy, A.: Framboidal and idiomorphic pyrite in the upper Maastrichtian sedimentary rocks at Gabal Oweina, Nile Valley, Egypt: Formation processes, oxidation products and genetic implications to the origin of framboidal pyrite, Geochim. Cosmochim. Ac., 90, 195–220, https://doi.org/10.1016/j.gca.2012.05.004, 2012.

Stock, J. M. and Lee, J.: Do microplates in subduction zones leave a geological record?, Tectonics, 13, 1472–1487, https://doi.org/10.1029/94TC01808, 1994.

Svensen, H., Planke, S., Malthe-Sørenssen, A., Jamtveit, B., Myklebust, R., Rasmussen Eidem, T., and Rey, S. S.: Release of methane from a volcanic basin as a mechanism for initial Eocene global warming, Nature, 429, 542–545, https://doi.org/10.1038/nature02566, 2004.

Svensen, H., Planke, S., Chevallier, L., Malthe-Sørenssen, A., Corfu, F., and Jamtveit, B.: Hydrothermal venting of greenhouse gases triggering Early Jurassic global warming, Earth Planet. Sc. Lett., 256, 554–566, https://doi.org/10.1016/j.epsl.2007.02.013, 2007.

Svensen, H., Planke, S., Polozov, A. G., Schmidbauer, N., Corfu, F., Podladchikov, Y. Y., and Jamtveit, B.: Siberian gas venting and the end-Permian environmental crisis, Earth Planet. Sc. Lett., 277, 490–500, https://doi.org/10.1016/j.epsl.2008.11.015, 2009.

Svensen, H., Aarnes, I., Podladchikov, Y. Y., Jettestuen, E., Harstad, C. H., and Planke, S.: Sandstone dikes in dolerite sills: Evidence for high-pressure gradients and sediment mobilization during solidification of magmatic sheet intrusions in sedimentary basins, Geosphere, 6, 211–224, https://doi.org/10.1130/GES00506.1, 2010.

Svensen, H. H., Hammer, Ø., Chevallier, L., Jerram, D. A., Silkoset, P., Polteau, S., and Planke, S.: Understanding thermogenic degassing in large igneous provinces: Inferences from the geological and statistical characteristics of breccia pipes in the western parts of the Karoo Basin, in: Mass Extinctions, Volcanism, and Impacts: New Developments, Geol. Soc. Am., 544, 67–84, https://doi.org/10.1130/2020.2544(03), 2020.

Sweeney, J. J. and Burnha, A. K.: Evaluation of a Simple Model of Vitrinite Reflectance Based on Chemical Kinetics, Bulletin, 74, 1559–1570, https://doi.org/10.1306/0C9B251F-1710-11D7-8645000102C1865D, 1990.

Teske, A., Lizarralde, D., and Höfig, T. W.: Expedition 385 Scientific Prospectus: Guaymas Basin Tectonics and Biosphere: feedbacks between continental rifting, magmatism, sedimentation, thermal alteration of organic matter, and microbial activity, International Ocean Discovery Program, https://doi.org/10.14379/iodp.sp.385.2018, 2018.

Teske, A., Lizarralde, D., Höfig, T. W., Aiello, I. W., Ash, J. L., Bojanova, D. P., Buatier, M. D., Edgcomb, V. P., Galerne, C. Y., Gontharet, S., Heuer, V. B., Jiang, S., Kars, M. A. C., Khogenkumar Singh, S., Kim, J.-H., Koornneef, L. M. T., Marsaglia, K. M., Meyer, N. R., Morono, Y., Negrete-Aranda, R., Neumann, F., Pastor, L. C., Peña-Salinas, M. E., Pérez Cruz, L. L., Ran, L., Riboulleau, A., Sarao, J. A., Schubert, F., Stock, J. M., Toffin, L. M. A. A., Xie, W., Yamanaka, T., and Zhuang, G.: Expedition 385 summary, in: Guaymas Basin Tectonics and Biosphere, edited by: Teske, A., Lizarralde, D., Höfig, T. W., and the Expedition 385 Scientists, Proceedings of the International Ocean Discovery Program, 385: College Station, TX, International Ocean Discovery Program, https://doi.org/10.14379/iodp.proc.385.101.2021, 2021a.

Teske, A., Lizarralde, D., Höfig, T. W., Aiello, I. W., Ash, J. L., Bojanova, D. P., Buatier, M. D., Edgcomb, V. P., Galerne, C. Y., Gontharet, S., Heuer, V. B., Jiang, S., Kars, M. A. C., Khogenkumar Singh, S., Kim, J.-H., Koornneef, L. M. T., Marsaglia, K. M., Meyer, N. R., Morono, Y., Negrete-Aranda, R., Neumann, F., Pastor, L. C., Peña-Salinas, M. E., Pérez Cruz, L. L., Ran, L., Riboulleau, A., Sarao, J. A., Schubert, F., Stock, J. M., Toffin, L. M. A. A., Xie, W., Yamanaka, T., and Zhuang, G.: Expedition 385 methods, in: Guaymas Basin Tectonics and Biosphere, edited by: Teske, A., Lizarralde, D., Höfig, T. W., and the Expedition 385 Scientists, Proceedings of the International Ocean Discovery Program, 385: College Station, TX, International Ocean Discovery Program, https://doi.org/10.14379/iodp.proc.385.102.2021, 2021b.

Teske, A., Lizarralde, D., Höfig, T. W., Aiello, I. W., Ash, J. L., Bojanova, D. P., Buatier, M. D., Edgcomb, V. P., Galerne, C. Y., Gontharet, S., Heuer, V. B., Jiang, S., Kars, M. A. C., Khogenkumar Singh, S., Kim, J.-H., Koornneef, L. M. T., Marsaglia, K. M., Meyer, N. R., Morono, Y., Negrete-Aranda, R., Neumann, F., Pastor, L. C., Peña-Salinas, M. E., Pérez Cruz, L. L., Ran, L., Riboulleau, A., Sarao, J. A., Schubert, F., Stock, J. M., Toffin, L. M. A. A., Xie, W., Yamanaka, T., and Zhuang, G.: Site U1545, in: Guaymas Basin Tectonics and Biosphere, edited by: Teske, A., Lizarralde, D., Höfig, T. W., and the Expedition 385 Scientists, Proceedings of the International Ocean Discovery Program, 385: College Station, TX (International Ocean Discovery Program), https://doi.org/10.14379/iodp.proc.385.103.2021, 2021c.

Tomkins, A. G.: Windows of metamorphic sulfur liberation in the crust: Implications for gold deposit genesis, Geochim. Cosmochim. Ac., 74, 3246–3259, https://doi.org/10.1016/j.gca.2010.03.003, 2010.

Toulmin, P. and Barton, P. B.: A thermodynamic study of pyrite and pyrrhotite, Geochim. Cosmochim. Ac., 28, 641–671, https://doi.org/10.1016/0016-7037(64)90083-3, 1964.

Wang, D., Lu, X., Zhang, X., Xu, S., Hu, W., and Wang, L.: Heat-model analysis of wall rocks below a diabase sill in Huimin Sag, China compared with thermal alteration of mudstone to carbargilite and hornfels and with increase of vitrinite reflectance: Heat-Model Analysis Of Wall Rocks, Geophys. Res. Lett., 34, 16, https://doi.org/10.1029/2007GL030314, 2007.

Wang, H. and Salveson, I.: A review on the mineral chemistry of the non-stoichiometric iron sulphide, Fe $1 - xS$ ($0 \leq \times \leq 0.125$): polymorphs, phase relations and transitions, electronic and magnetic structures, Phase Trans., 78, 547–567, https://doi.org/10.1080/01411590500185542, 2005.

Wehland, F., Alt-Epping, U., Braun, S., and Appel, E.: Quality of pTRM acquisition in pyrrhotite bearing contact-metamorphic limestones: possibility of a continuous record of Earth magnetic field variations, Phys. Earth Planet. Int., 148, 157–173, https://doi.org/10.1016/j.pepi.2004.08.008, 2005.

Welton, J. E.: SEM petrology atlas, Tulsa, Oklahoma: American Association of Petroleum Geologists, Vol. 4, https://doi.org/10.1306/Mth4442, 1984.

White, J., McPHie, J., and Skilling, I.: Peperite: a usefull genetic term, J. Volcanol. Geotherm. Re., 114, 1–17, https://doi.org/10.1016/S0377-0273(01)00278-5, 2000.

Wilkin, R. T. and Barnes, H. L.: Formation processes of framboidal pyrite, Geochim. Cosmochim. Ac., 61, 323–339, https://doi.org/10.1016/S0016-7037(96)00320-1, 1997.

Winkler, H. G. F. and Winkler, H. G. F.: Metamorphism of Pelites. Petrogenesis of Metamorphic Rocks, 206–238, https://doi.org/10.1007/978-1-4757-4215-2_14, 1979.

Winter, J. D.: Metamorphic Grades, Zones, Facies and Facies Series, in: Encyclopedia of Geology, Elsevier, 439–444, https://doi.org/10.1016/B978-0-08-102908-4.00034-5, 2021.

Yallup, C., Edmonds, M., and Turchyn, A. V.: Sulfur degassing due to contact metamorphism during flood basalt eruptions, Geochim. Cosmochim. Ac., 120, 263–279, https://doi.org/10.1016/j.gca.2013.06.025, 2013.

Zhao, C., Hobbs, B. E., and Ord, A.: Convective and advective heat transfer in geological systems, Springer, Berlin Heidelberg, 229 pp., 2008.

Zucchi, M., Tursi, F., Brogi, A., Liotta, D., Spiess, R., Caggianelli, A., Ventruti, G., and Langone, A.: Syn-tectonic contact aureole and metasomatic reaction zones in carbonate and pelitic host rocks (Elba Island, Italy), Tectonophysics, 853, 229782, https://doi.org/10.1016/j.tecto.2023.229782, 2023.

Zürcher, L. and Kring, D. A.: Hydrothermal alteration in the core of the Yaxcopoil-1 borehole, Chicxulub impact structure, Mexico, Meteor. Planet. Sci., 39, 1199–1221, https://doi.org/10.1111/j.1945-5100.2004.tb01137.x, 2004.